Department of Physics and Astronomy
Heidelberg University

Bachelor Thesis in Physics
submitted by

David Kuhn

born in Heidelberg (Germany)

2024

Leakage Currents in High Voltage Monolithic Active Pixel Sensors in the context of the LHCb Upgrade II MightyTracker

This Bachelor Thesis has been carried out by David Kuhn at the
Physikalisches Institut in Heidelberg
under the supervision of
Prof. Ulrich Uwer

Abstract:

During the Long Shutdown 4 of the LHC the LHCb tracking system is planned to receive various major upgrades. The MightyTracker will replace the current Scintillating Fibre tracker to cope with the instantaneous luminosity increase at the interaction point that is planned for the LHC High Luminosity era. This subdetector consists of an outer part, which will still utilize scintillating fibers, while the inner part of it is based on silicon pixel detectors, in particular HV-MAPS.
In this context, several HV-MAPS prototypes are used to study the leakage current of the pixel under various temperature and radiation conditions.
The IV characteristic is analyzed and the source of leakage current determined by fitting a model that takes thermal excitations and trap assisted tunneling into account. It is concluded that the main source of leakage current is within the depleted volume in the pixel matrix. For the leakage current and breakdown voltage a temperature dependence is observed, which is compatible with the predicted dependence. From this temperature dependence the effective energy E_a is determined. At low bias voltages an effective energy E_a, which is compatible with the expectations, is observed. The observed effective energy decreases with increasing bias voltage, which can be explained by trap assisted tunneling. Additionally, the influence of TID damage on the leakage current is studied. During the irradiation an increase in the leakage current and decrease of the pixel guard ring potential is observed. A possible explanation for the observed effects is discussed.

Zusammenfassung:

In der 4. Wartungspause des LHCs soll das Spurrekonstruktionssystem des LHCb aufgerüstet werden. Eines der zentralen Upgrades stellt dabei der MightyTracker dar. Dieser wird den aktuell betriebenen Szintallationsfaserdetektor ersetzen, um die höhere instantane Luminosität, die in der LHC High Luminosity Ära geplant ist, verarbeiten zu können. Der MightyTracker soll aus zwei Teilen bestehen. Im äußeren Teil soll weiterhin auf szintillierende Fasern gesetzt werden, während im inneren Teil Halbleiterpixeldetektoren, im speziellen HV-MAPS, zum Einsatz kommen sollen.
Dafür werden verschiedene HV-MAPS Prototypen genutzt, um den Leckstrom des aktiven Diodenparts unter verschiedenen äußeren Temperatur- und Strahlungseinflüssen zu untersuchen.
Die Ursachen des Leckstroms werden bestimmt, indem ein theoretisches Modell an die IV Charakteristik angepasst werden. Das Modell enthält thermische Anregungen, sowie Trap assistieretes Tunneln. Dabei wird geschlussfolgert, dass der Großteil des Leckstroms im veramten Volumen, innerhalb der Pixelmatrix, seinen Ursprung hat. Eine Temperaturabhängigkeit des Leckstroms und der Breakdownspannung wird beobachtet. Diese stimmt mit der erwarteten Abhängigkeit überein. Darüber hinaus wird aus der Temperaturabhängigkeit des Leckstroms die effektive Energie E_a bestimmt. Für niedrige Biasspannungen stimmt diese mit dem erwarteten Wert überein. Für höhere Biasspannungen fällt der Wert der effektiven Energie ab, was mit Trap assistiertem Tunneln erklärt wird.
Der Einfluss von TID Schäden auf den Leckstrom wird ebenfalls untersucht. Dabei wird festgestellt, dass während der Bestrahlung mit Röntgenstrahlen der Leckstrom ansteigt und das Potential am Pixelguardring abfällt. Für diese Effekte wird eine mögliche Erklärung diskutiert.

Contents

1 Introduction

The currently best understanding of the fundamental particles and interactions that make up our universe is the Standard Model of particle physics (SM). The SM has proven its validity in many different experiments, where its predictions have been tested and measured to a high degree of certainty. Prominent examples being the correct prediction of the existence and the mass of the Higgs boson [1], which has been discovered by two detectors at the Large Hadron Collider (LHC) in 2012 [2, 3]. Though the SM is the best model in existence, it is known that it is not complete. Certain effects like the matter-antimatter asymmetries [4] or neutrino masses [5] that have been observed, can not be explained within the SM. To further refine our understanding of the fundamental particles and their interactions, the LHC will be operated at higher instantaneous luminosity [6].
In this quest for new physics also the LHCb (large hadron collider beauty) experiment is planned to get its second upgrade in 2034. The upgrade will enable a deep looks into many aspects of flavour-physics and low energy QCD [7]. For the Upgrade II it is proposed to replace the current downstream tracking system, the **SCI**ntillating **FI**bre tracker (SCIFI) with the MightyTracker. The MightyTracker will consist of two seperate parts. In the outer regions, where the granularity and radiation hardness of the scintillating fibers are still sufficient to cope with higher particle flux, scintillating fibers will be used. In the center, close to the beam pipe, where a much higher particle rate is expected, it is proposed to use silicon pixel detectors, which show a much higher radiation hardness and with their higher granularity can cope with higher particle multiplicities. **H**igh **V**oltage **M**onolithic **A**ctive **P**ixel **S**ensor (HV-MAPS) [8] are the proposed technology for this part. HV-MAPS are produced in commercial HV-CMOS processes which makes them rather cost effective. The sub-detector will consist of individual chips, each equipped with many individual pixels. Each pixel consists of a depleted diode for particle detection and parts of the front end electronics used to digitize the created signal. This monolithic structure allows for a smaller material budget than hybrid pixel sensors.
In this thesis the leakage currents of the charge collecting diodes, which greatly affects the noise level in he detector, in different types of HV-MAPS will be investigated. For this, several different prototypes with slightly different designs will be examined. The IV characteristic, the leakage current as a function of the applied high voltage is investigated. Additionally, the impacts of changing temperature and ionizing radiation are studied. In the second section of this thesis the LHCb experiment will be discussed in more detail. This section is followed by a short introduction into semiconductors and how they can be utilized to detect particles. In the fourth section a short introduction in the different setups, used for all measurements within this thesis is given. The fifth section provides insights in the general behavior of the leakage currents for different bias voltages. Section 6 deals with the observed temperature effects, while in section 7 the influence of ionizing radiation, in this case X-rays is discussed. In the last section a short summary of all measurements and results is given, alongside with an outlook on how these methods can be refined and used to characterize HV-MAPS.

2 The LHCb Experiment

The LHCb experiment is a single-arm forward spectrometer, which is specialized to analyze the decays of B- and D- hadrons. The experiment is located at one of the interaction points of the 27 km long circular proton-proton collider LHC located at CERN. The p-p collisions happen with a center of mass energy $\sqrt{s} = 13.6\,\text{TeV}$. As the, for LHCb interesting, particles are predominantly created in processes with small angles with respect to the beam pipe, the forward structure with opening angles of 250 mrad in the vertical and 300 mrad in the horizontal plane is perfectly suited for these kinds of analysis. The detector consists of various sub-detectors, which either are used to track particle trajectories or are part of the particle identification (PID) system. In Figure 1 a schematic side-view of the whole detector is shown. The current tracking system consists of the vertex locator (VELO), the upstream tracker (UT) and the SciFi tracker. The interaction point of the proton beams is located inside VELO. The heavy particles (like B- and D- hadrons) that are created at the collision point have very short lifetimes and decay in the VELO. The main purpose of the VELO is to determine the vertex of these decays. With the tracking system down- and upstream of the magnet it is possible to determine the bending of charged particle tracks in the magnetic field. With that it is possible to determine the momentum of the particles. The PID system consists of the RICH 1 and 2, which are ring imaging Cerenkov detectors, as well as the hadronic and electromagnetic calorimeters at the back. Additionally, several muon stations are present within the detector. The PID system measures the energy of the particles which together with informations about their charge and momentum provides the ability to identify these particles.

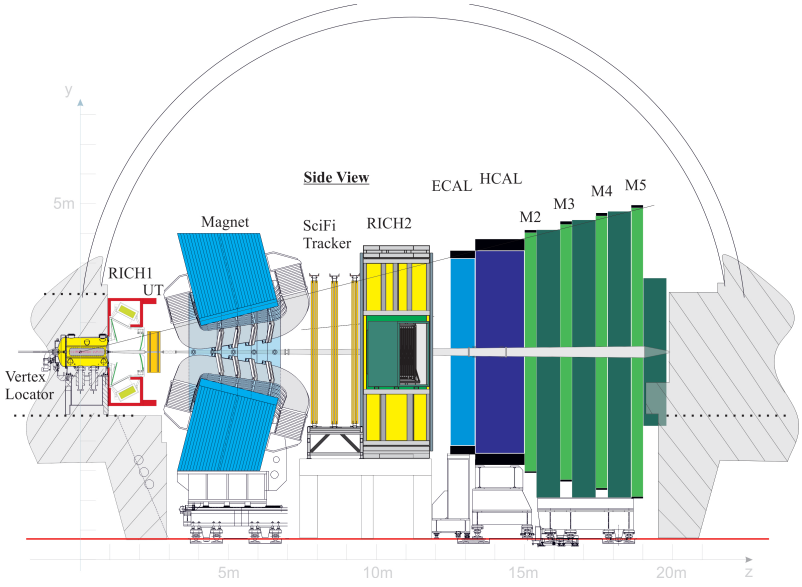

Figure 1: Schematic side-view of the current LHCb detector. [9]

As the VELO is used to measure the decay of the heavy hadrons with a very short lifetime, it needs to be placed as close as possible to the interaction point. For that purpose it is split into two movable components on either side of the beam pipe. To prevent radiation damage during unstable beams the VELO is moved away from the

interaction points during phases, where no data is taken. The VELO utilizes hybrid silicon pixel detectors.
In both the RICH1 and RICH2, the emission angle of Cherenkov radiation is utilized in identifying particles. This type of radiation is produced by particles traversing material at a higher speed than the speed of light in this material. To detect the Cherenkov photons, photo multiplier tubes are used.
The UT utilizes 4 layers of silicon strip detectors that each cover an area of $2\,\mathrm{m}^2$. The second and third layer of the UT are tilted $\pm 5^\circ$ with respect to the first and fourth layer to achieve a 2D resolution.
The SciFi tracker utilizes scintillating fibers with a diameter of $250\,\mu\mathrm{m}$. These fibers produce scintillating light from traversing particles, which produces a signal in silicon photo multipliers located at the end of the fibers. Each of the three SciFi stations consists of 4 layers of fibers, using a similar layout as the UT. Each layer has an active area of about $30\,\mathrm{m}^2$ [9].
The electronic and hadronic calorimeters consist of alternating layers of absorber and scintillating tiles. Traversing electromagnetic/strong interacting particles produce showers in the absorber, which are detected with the scintillating tiles. The amount of scintillation light is proportional to the energy of the traversing particles.
The muon stations are able to identify muon candidates. Absorbers between the different muon stations are able to filter out hadrons, so only muons can traverse all 4 of these stations. Multi wire proportional chambers are used to identify the penetration depth and tracks of the muon candidates. [9]

2.1 Physics at LHCb

The standard model of particle physics (SM) is a quantum field theory that describes the fundamental particles and their interactions. The fundamental particles can be divided into 12 different fermions and gauge bosons, which mediate the forces. The fermions, which all carry a spin of $\frac{1}{2}$ can be divided into 6 quarks and 6 leptons. The fermions can be divided into 3 generations each consisting of an up type (charge of $+\frac{2}{3}$) and down type quark (charge of $-\frac{1}{3}$). In addition to the 2 quarks, each generation also contains 2 leptons, a charged lepton (electron, muon, tauon) and their respective chargeless neutrino. The generations only differ by the mass of their respective particles. The generational structure and mass difference can not be explained within the SM.
In the standard model the fundamental forces are carried via gauge bosons with the spin of 1 [10]. The electromagnetic force is mediated by the massless photon γ, the gauge bosons of the strong interactions are eight also massless gluons g. The weak interaction is mediated by the charged and massive $W^\pm$ and the neutral Z-bosons. In addtion the Higgs boson with a spin of 0 generates the mass of the massive particles by electroweak symmetry breaking [1]. The particles of the SM are shown in Figure 2.

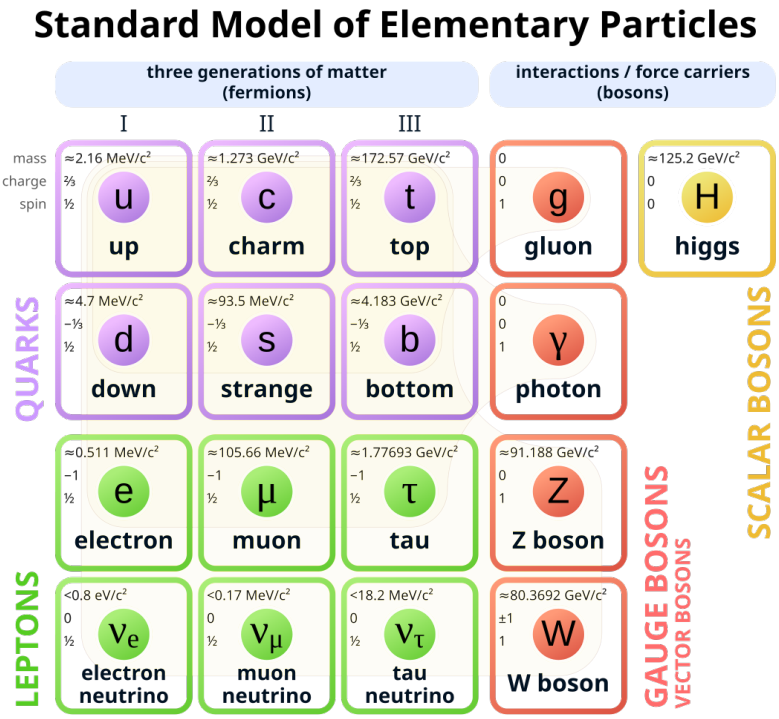

Figure 2: The fundamental particles that make up the standard model. [11]

Within the standard model flavour changes between quarks are only allowed in a weak process that includes a W-boson. The mixing of the flavours in the weak interaction is described by the so called Cabibbo-Kobayashi-Maskawa (CKM) Matrix [12, 13]. This is a unitary matrix that can be parameterized using 3 mixing angles and a CP violating phase. One goal of the LHCb experiment is to determine these parameters to a high accuracy. Also flavour changing processes beyond the standard model are within the scope of LHCb.

2.2 LHCb Upgrade II

In the 4th long shutdown (LS4) of the LHC, the LHCb detector is planned to receive its Upgrade II to cope with the increase in instantaneous and integrated luminosity. For Run 5 and 6, which are following the LS4, an integrated luminosity of $350\,\mathrm{fb}^{-1}$ is expected. The instantaneous luminosity is expected to rise up to $1.5 \times 10^{34}\,\mathrm{cm}^{-2}\,\mathrm{s}^{-1}$. For this the rate and radiation hardness capability of the various subdetectors will need to increase. A schematic of the LHCb detector after the second upgrade in the LS4 is shown in Figure 33.

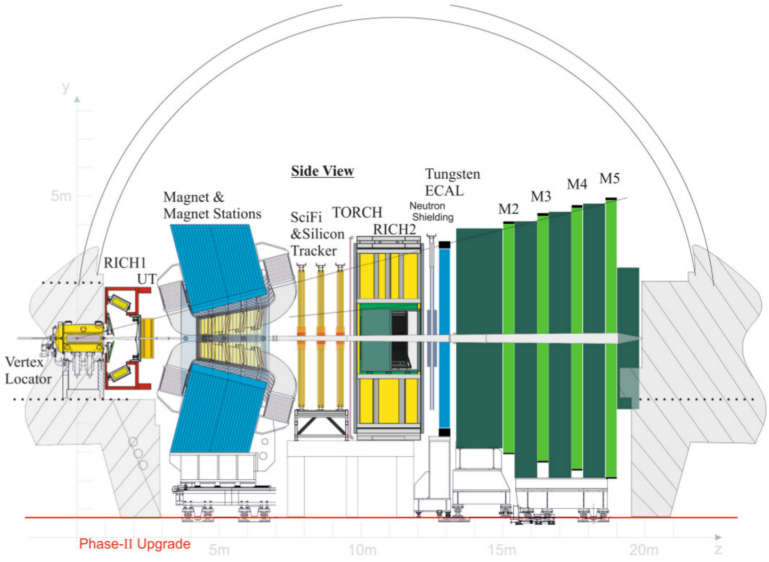

Figure 3: Schematic side-view of the LHCb Upgrade II detector. [14]

In Upgrade II the tracking system of LHCb will consist of VELO, UT and the MightyTracker, an successor of the SciFi tracker. Additional tracking stations in the magnet will allow to track the paths of low momentum particles, which are not able to reach the MightyTracker. The PID system will also undergo various changes and upgrades in detectors. The hadronic calorimeter will no longer be needed, as it was mainly used for the hardware trigger, which was already replaced by a software trigger in Upgrade I, and will be replaced by additional absorber material, to increase the efficiency of the muon stations downstream. The additional proposed Time of internally reflected Cherenkov radiation (TORCH) will offer additional PID capabilities for low momentum particles.

2.3 The MightyTracker

This thesis is mainly focused on the development of silicon pixel detectors for the proposed MightyTracker (MT), which is now explained in more detail. The general layout of the MT was already discussed earlier. To cope with the increased rate and radiation damage, that is expected in the high luminosity era of LHC, the SciFi tracker needs to be upgraded. The granularity and radiation hardness of the SciFi are not sufficient in the inner regions close to the beam pipe. For this region it is proposed to use silicon pixel detectors, which are able to fulfill the radiation hardness and granularity requirements given in [15].
The layout of the detector will still consist of 3 stations, like it is the case with the current SciFi tracker. Each station will host 4 SciFi like detection layers, of which two of them are vertical ('X-layers') and the other are tilted by $\pm 5°$ ('U-' and 'V-layers') [14]. Additionally each station will feature two layers of silicon pixel detectors in the central region. The layout of one such station is shown in Figure 4.

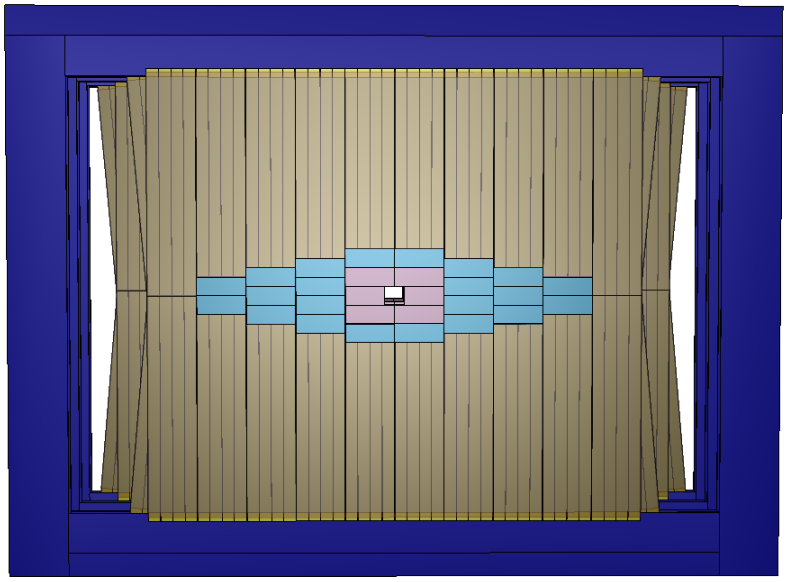

Figure 4: Layout of one of the MT stations. The central region is covered with silicon pixel detectors (pink and blue), while the outer region will utilize scintillating fibre technology. [14]

The proposed technology for the silicon pixel detectors are HV-MAPS [8].

3 Silicon Pixel Detectors

3.1 Interaction of charged Particles and Photons in Matter

The aim of the MightyTracker is to reconstruct the trajectory of charged particles. For this the charged particles need to interact with the detector. Additionally to this charged particle interaction, photon interactions with matter are described in this section, as this is relevant for the X-ray irradiation studies.
Charged particles like protons, electrons and pions interact with matter through different processes described subsequently.

Ionization

While traversing material, charged particles will deposit a part of their energy in the material. This energy deposition is based on ionization, where shell electrons of atoms in the material receive enough energy from the traversing particle to reach an unbound state. The energy loss through ionization of the traversing material can be described by the *Bethe-Bloch-formula* [16]:

$$-\frac{1}{\rho}\left\langle\frac{\mathrm{d}E}{\mathrm{d}x}\right\rangle = \frac{KZz^2}{A\beta^2}\left[\frac{1}{2}\ln\left(\frac{2m_e c^2\beta^2\gamma^2 E_{max}}{I^2}\right)-\beta^2\right] \tag{3.1}$$

$\left\langle\frac{\mathrm{d}E}{\mathrm{d}x}\right\rangle$ describes the mean energy loss per distance dx traveled in the material with density ρ and is dependent on a constant K ($K = 307\,\mathrm{keVcm^2/mol}$), Z the atomic number of the ionized material, z the charge of the incoming particle in units of the elementary charge e and A $[\mathrm{g\,mol^{-1}}]$ the atomic mass of the material. Furthermore it depends on the electron mass m_e, the speed of light c, as well as the maximal energy transfer E_{max} to the material and its mean ionization energy I. It also dependens on the Lorentz factor $\gamma = [1-\beta]^{-1/2}$ and the velocity β of the incoming particle. This is depicted in Figure 5. The Bethe-Bloch formula is only valid for $0.1 < \beta\gamma < 1000$, outside of this region corrections must be made, which will not be discussed here, but can be found in [16, 17] For electrons (and positrons) the Bethe-Bloch formula is not sufficient to describe the energy loss in matter. The predominant process for electrons at energies $> \mathcal{O}(10\,\mathrm{MeV})$ is *Bremsstrahlung* [16].

Bremsstrahlung

Bremsstrahlung is an effect that relies on the electromagnetic interaction between high relativistic, low mass particles and the Coulomb field of atomic nuclei in the material. During this interaction a photon is emitted by the traversing, charged particle. This type of energy loss is described by:

$$-\frac{\mathrm{d}E}{\mathrm{d}x} = \frac{E}{X_0} \tag{3.2}$$

with a material specific constant, the radiation length X_0. The photons coming from Bremsstrahlung can then again interact with the material they are produced in. Bremsstrahlung is dominant for the energy loss of high energy ($E > \mathcal{O}(10\,\mathrm{MeV})$) electrons in matter.

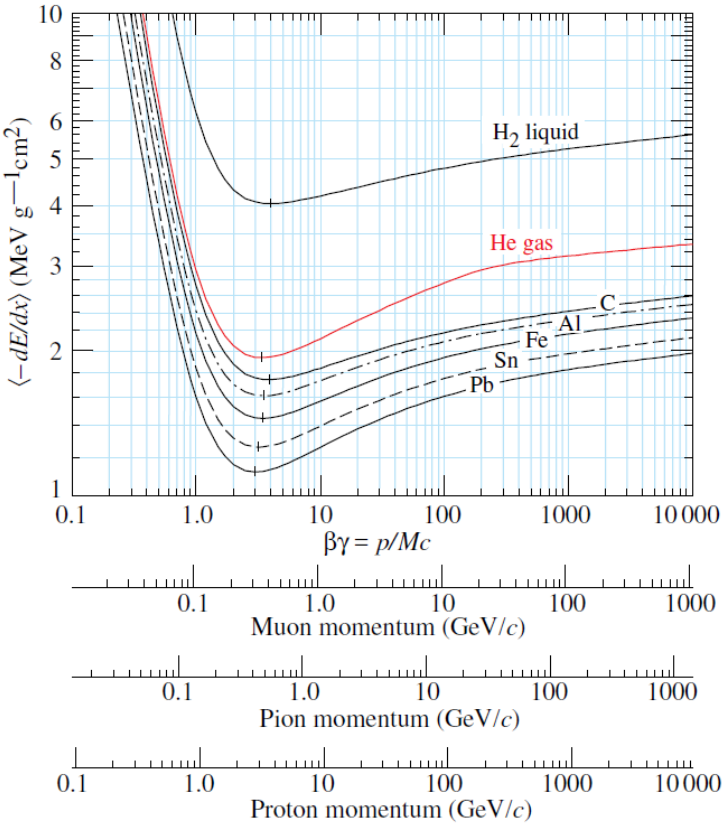

Figure 5: Mean energy loss by ionization as a function of $\beta\gamma$ as well as the respective momentums of muons, pions and protons. [16]

Photon interactions

Photons have several different types of interactions in matter. They can either be absorbed by shell electrons in the material, which leads to ionization of the atom. Other options are inelastic Compton scattering, where the photon only loses a part of its energy and e^+e^--pair production, which happens only for $E_\gamma > 2m_e c^2$. The photon absorption is the most relevant for this thesis, and is therefore discussed in more detail. The absorption of photons is based on the photoelectric effect, where photons get absorbed by shell electrons in the material. In the process an electron gets excited to an higher energy state. The cross section σ, that describes the absorption process is given by:

$$\sigma \propto \frac{Z^5}{E_\gamma^{7/2}} \tag{3.3}$$

and depends on the photon energy E_γ and the atomic number Z of the material [17].

3.2 Semiconductors

As this thesis revolves around particle detection based on semiconductors, a short introduction into semiconductors and leakage currents in semiconductors will be given.
All solid materials can be divided into 3 groups with respect to their electrical conductivity: conductor, insulator and semiconductor. Conductors have a typical conductivity of $< 1 \times 10^{-8}\,\Omega^{-1}\,\mathrm{cm}^{-1}$, while for insulators the conductivity is typically $> 1 \times 10^{3}\,\Omega^{-1}\,\mathrm{cm}^{-1}$, the conductivity of semiconductors lies in between [17]. Commonly used materials for semiconductors are silicon and germanium as pure elements. Besides that there also are compound materials like gallium arsenide or gallium phosphide. In HV-MAPS mainly silicon is used, therefore the discussion here is restricted to silicon. The energy level of single atoms in the lattice can not be described fully on its own. However, the energy level of electrons in the crystal can be described by so-called *energy bands*. Energy levels of electrons in the same band are typically in the range of a few meV [17, 18]. This allows electrons in the same energy band to easily transition to unoccupied energy levels within the same band.

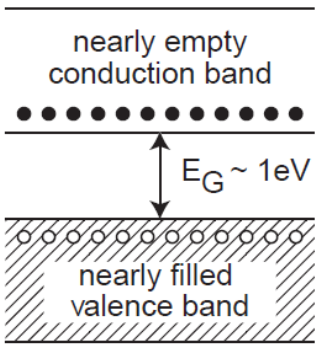

Figure 6: Schmeatic band strucutre of Si. [17]

In thermal equilibrium at temperature T the occupation of states with energy E is

given by a *Fermi-Dirac distribution*:

$$f_n(E,T) = \left[\exp\left(\frac{E-E_F}{k_B T}\right)+1\right]^{-1}. \tag{3.4}$$

E_F is the Fermi energy and k_B the Boltzmann constant. At $T = 0\,\mathrm{K}$ all states below E_F are fully occupied, while all states above are unoccupied. The two bands on either side of the Fermi energy level are called *valence* and *conduction* band. The conduction band is energetically above the valence band. The energy gap $E_g = E_C - E_V$ between the lowest conduction (E_C) and highest valence (E_V) band energy level is quite small in semiconductors (1.17eV in Si at 0K, [18]). The band structure is shown in Figure 6. This makes it possible, that thermal excitation and external electric fields promote electrons from the valence to the conduction band which leads to free electrons in the conduction band. As the size E_G of the band gap is closely related to the lattice spacing, temperature and pressure will have an influence. The energy gap of silicon for example decreases from 1.17eV at 0K down to 1.12eV at 300K [18].
If electrons are promoted into the conduction band, they leave behind a positively charged 'hole' in the valence band. As this hole can easily be filled by another electron from the valence band, it needs to be treated like a (in the valence band) free moving positive charge, which will also contribute to the conductivity of the semiconductor.
The conductivity σ of an intrinsic semiconductor is therefore given by:

$$\sigma = e(n\mu_n + p\mu_p) \tag{3.5}$$

n and p describe the charge carrier density of electrons (n) and holes (p), while μ_i describes their mobility. To obtain the charge carrier density of a semiconductor the density of states of the holes/electrons $D_{n/p}(E)$ times their respective occupation probability $f_{n/p}(E,T)$ needs to be integrated. The density of states is obtained by approximating the free charge carriers as a free electron gas, where instead of the electron mass an effective mass for the electrons $m_n^\star$ and holes $m_p^\star$ and the reduced Planck's constant $\hbar$ are used [18].

$$D_n(E) = \frac{1}{2\pi^2}\left(\frac{2m_n^\star}{\hbar^2}\right)^{\frac{3}{2}}\sqrt{E-E_C} \tag{3.6}$$

$$D_p(E) = \frac{1}{2\pi^2}\left(\frac{2m_p^\star}{\hbar^2}\right)^{\frac{3}{2}}\sqrt{E_V-E} \tag{3.7}$$

The occupation of the bands is obtained from (3.4). A commonly used assumption is that the Fermi energy lies in the middle of the energy gap between valence and conduction band. With this the occupation probability of the electrons in the conduction band simplifies to:

$$f_n(E,T) = \exp\left(-\frac{E-E_F}{k_B T}\right) \tag{3.8}$$

as $|E - E_F| \gg k_B T$.
As the holes are the result of unoccupied electron state, their occupation probability is given by:

$$f_p(E,T) = 1 - f_n(E,T). \tag{3.9}$$

To now obtain n and p, the following integrals need to be carried out:

$$n = \int_{E_C}^{\infty} D_n(E) f_n(E,T) dE \tag{3.10}$$

$$p = \int_{-\infty}^{E_V} D_p(E) f_p(E,T) dE = \int_{-\infty}^{E_V} D_p(E)[1 - f_n(E,T)] dE \tag{3.11}$$

The limits of the integrals are given by the fact that electrons in the conduction band have a minimal energy of E_C, while the energy of holes in the valence band is limited by E_V.
Carrying out the integrals yields:

$$n = \underbrace{2\left(\frac{m_n^\star k_B T}{2\pi\hbar^2}\right)^{\frac{3}{2}}}_{=N_C} \exp\left(-\frac{E_C - E_F}{k_B T}\right) \tag{3.12}$$

$$p = \underbrace{2\left(\frac{m_p^\star k_B T}{2\pi\hbar^2}\right)^{\frac{3}{2}}}_{=N_V} \exp\left(-\frac{E_F - E_V}{k_B T}\right). \tag{3.13}$$

where then N_C and N_V can be defined as the effective density of states in the conduction and valence band respectively. For silicon these effective densities at 300 K are:

$$N_C \approx 3.05 \times 10^{19} \mathrm{cm}^{-3} \tag{3.14}$$

$$N_V \approx 2.55 \times 10^{19} \mathrm{cm}^{-3} \tag{3.15}$$

In a thermal equilibrium the generation and recombination of electron-hole-pairs are in balance which means:

$$np = n_i^2 = const. \tag{3.16}$$

From that a temperature dependence of the intrinsic charge carrier can be deduced using (3.12):

$$\begin{aligned} n_i^2 &= N_C N_V \exp\left(-\frac{E_C - E_V}{k_B T}\right) = N_C N_V \exp\left(-\frac{E_G}{k_B T}\right) \\ &\propto T^{\frac{3}{2}} \exp\left(-\frac{E_G}{2k_B T}\right) \end{aligned} \tag{3.17}$$

The intrinsic charge carrier density does not depend on the Fermi energy.

3.2.1 Doping

If one calculates the intrinsic conductivity of semiconductors it occurs, that the conductivity is way to small for any application ($\mathcal{O}(1 \times 10^{-4}\,\Omega^{-1}\,\mathrm{m}^{-1})$). Therefore it is necessary to dope semiconductors to increase their conductivity and widely extend their usage in applications.
This doping is done by introducing impurities into the silicon. Silicon is a tetravalent atom, so by introducing a pentavalent impurity (commonly Phosphorus, Arsenic or Antimony) only 4 of the 5 valence electrons of the pentavalent atom can be bound in covalent bonds. The remaining electron remains loosely bound to the impurity

atom, but can easily be freed by a thermal excitation, even at room temperature. This now free electron will contribute to the conductivity of the semiconductor. The pentavalent atom is called *donor*. A similar behavior is observed when a trivalent, so called *acceptor* atom like Boron is placed in the lattice. Instead of supplying an additional electron to the semiconductor, it will create a hole by trapping an electron. This hole can be seen as a positive charge carrier and will contribute to the conductivity. This fact is also shown in Figure 7.

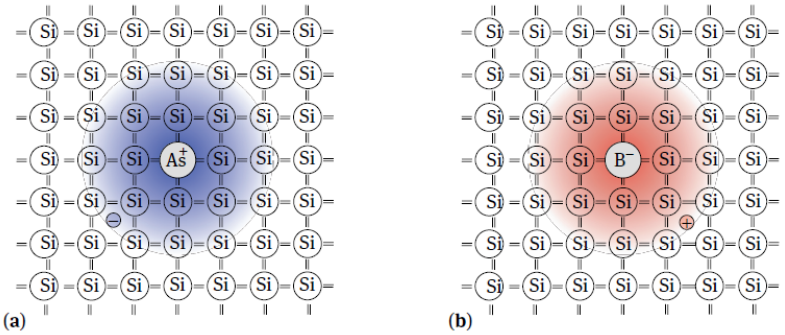

Figure 7: Doping atoms in a silicon lattice. (a) As as a donor atom (b) B as an acceptor atom [18]

Doped semiconductors are commonly called *extrinsic semiconductors*.
Semiconductors which are doped with a high concentration of donor atoms are called n-type semiconductor. Semiconductors which are doped with a high concentration of acceptor atoms are called p-type semiconductor [17]. The doping changes the charge carrier density in the semiconductors as well as the energy band structure. In a n-type semiconductor the energy level of the 5th valence electron in the donor atom E_D lies just under the conduction band. This creates new states which increases the Fermi energy $E_F \rightarrow E'_F$). This also changes the electron population densities in the conduction band. For an n-doped semiconductor one obtains:

$$\begin{aligned} n \approx n_D &= N_C \exp\left(-\frac{E_C - E'_F}{k_B T}\right) \\ &= N_C \exp\left(-\frac{E_C - E_F}{k_B T}\right) \exp\left(-\frac{E_F - E'_F}{k_B T}\right) \\ &= n_i \exp\left(\frac{E'_F - E_F}{k_B T}\right) \end{aligned} \tag{3.18}$$

Analogous the hole density changes to:

$$p \approx n_A = n_i \exp\left(\frac{E_F - E'_F}{k_B T}\right) \tag{3.19}$$

For p-doping these calculations are very similar and will not be shown here.

3.2.2 The p-n-junction

Semiconductor detectors are typically based on diodes. Diodes are junctions, where typically an n- and p-doped semiconductor are contacting.

In the n-doped part of the crystal the majority charge carriers are electrons and the Fermi level is close to the conduction band edge as shown in subsubsection 3.2.1, while in the p-doped part the situation is the opposite, the holes make up the majority of the charge carriers and the Fermi level is close to the valence band edge. Because of the high concentration gradient of holes and electrons a diffusion current occurs where holes diffuse (with diffusion current I_{diff}) into the n-doped part and electrons into the p-doped part, where they both recombine. The recombination leads to a formation of a charge carrier free zone at the p-n-junction, which is also called *depletion zone*. Since the atomic nuclei remain in the depletion zone, this zone is now charged and one speaks of a space charge. As the space charges in the p- and n-doped part are of opposite sign, an electric field forms. This electric field causes a drift current I_{drift}, which is opposing the diffusion current. An equilibrium state is reached for a high enough electric field at an equilibrium potential difference V_i. This effect is shown in Figure 8.

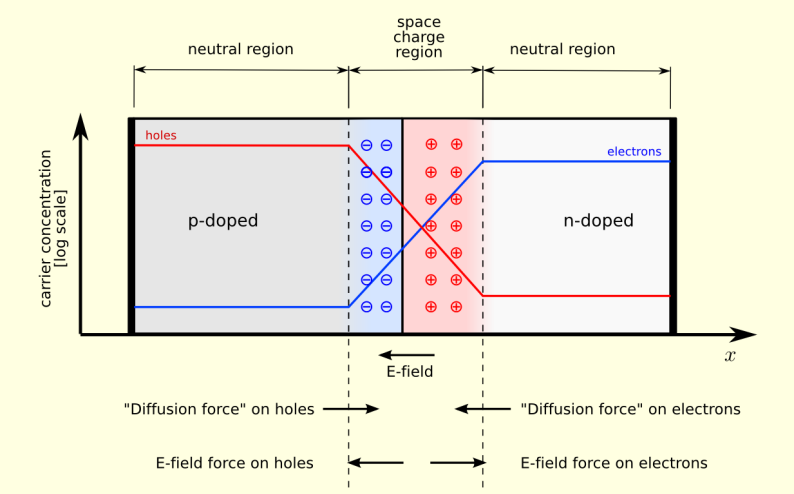

Figure 8: Schematic of a p-n-junction in equilibrium without an external voltage applied. [19]

If now an external bias voltage V_{bias} is applied, the depletion zone can either shrink or expand further into the material, depending on the polarity of the external voltage. Since the system is no longer in a thermal equilibrium, the statement made in (3.16) no longer holds true. Instead $np > n_i^2$ or $np < n_i^2$ need to be considered depending on the situation. The diode can either be driven with a forward bias ($V_p > V_n$) or in a reverse bias voltage($V_p < V_n$), where V_p and V_n are the potentials applied at the p- and n-doped part respectively. In the forward bias setting the electric field over the depletion zone and therefore also the drift current is reduced, which causes the depletion zone to shrink. In the case of a reverse bias voltage the exact opposite happens. The electric field becomes greater because of the increased potential difference between the p- and n-doped parts. This causes the drift current to get greater than the diffusion current, which then will cause the depletion zone to become wider. As semiconducting particle detectors utilize the depleted volume as detection volume, a reverse bias is used to achieve a great detection volume.
The situation is depicted in Figure 9, where also the energy band structure across the junction is shown.

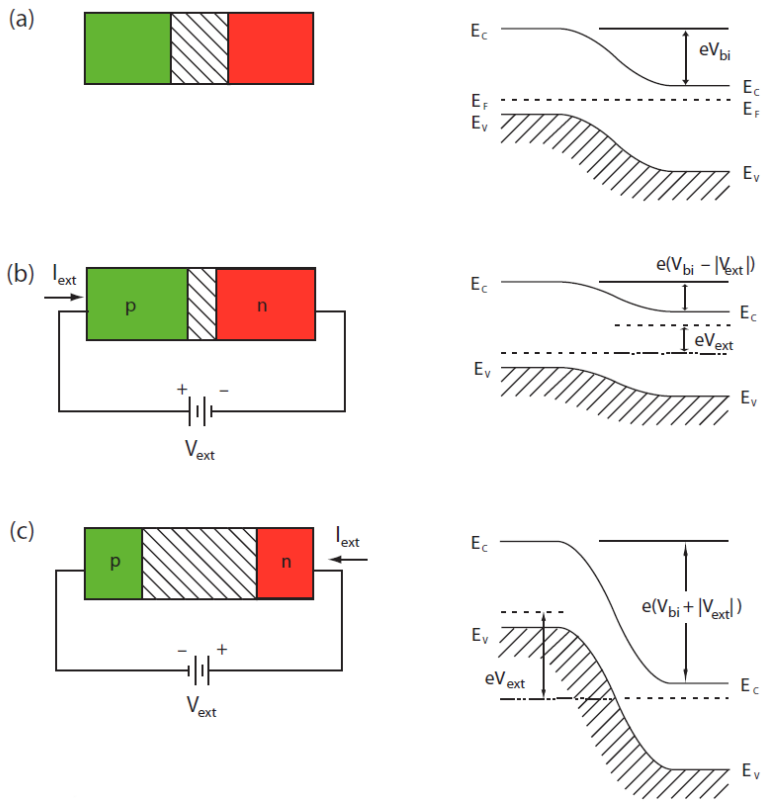

Figure 9: Diode with applied external voltage: (a) without external voltage. (b) external voltage in forward bias. (c) external voltage in reverse bias. Adapted from [17]

While the depletion zone is free of charge carriers, the adjacent regions feature a space charge, as the remaining atomic nuclei are charged. The space charge density in this regions can be approximated to be constant in the p-/n- doped regions. With this information, it is possible to calculate the width of the depletion zone by applying Maxwell's equations. This is done in [17] and will not be carried out here. The result of the calculations is that the depletion zone depth d is given by:

$$\begin{aligned} d_n &\approx 0.55\sqrt{\rho[\Omega\,\mathrm{cm}]V[\mathrm{V}]}\mu\mathrm{m} \\ d_p &\approx 0.32\sqrt{\rho[\Omega\,\mathrm{cm}]V[\mathrm{V}]}\mu\mathrm{m} \end{aligned} \tag{3.20}$$

in an n- or p-doped region respectively. The different numerical prefactors are due to the different mobilities of holes/electrons. ρ is the resistivity of the substrate, which depends on the doping concentration.

3.3 Leakage Currents in Semiconductors

In reverse biased diodes a leakage current I_L is observed. This leakage current can be generated by volume and by surface effects [17]. The dominant volume based I_L is produced by thermally generated electron-hole-pairs in the depletion zone. Impurities act as generation/recombination centres in the band gap [20]. This leakage current is proportional to the depleted volume Ad, where A is the area of the depleted zone

and d the depletion depth. For the leakage current then follows with (3.20):

$$I_L \propto Ad\frac{n_i}{\tau_g} \propto \sqrt{V_{bias}}\frac{n_i}{\tau_g}. \tag{3.21}$$

τ_g is the charge carrier generation lifetime, which is a time constant that describes the average time needed for generated charge carriers to return back in the equilibrium state [17]. As the trapping cross section is dependent on the thermal velocity the relation $\tau_g \propto \frac{1}{T^{1/2}}$ is obtained [17]. With this relations and (3.17) one obtains:

$$I_L \propto T^2 \exp\left(-\frac{E_a}{2k_B T}\right) \tag{3.22}$$

where E_a is a parameter called *effective energy*. Experimentally this value is measured to $E_a = 1.21\text{eV}$ [21].
Surface effects mostly originate from the fabrication process of the chips, from damage or depositions on the surface. In most cases surface effects on the leakage current are dominated by volume effects [17].

3.3.1 Breakdown voltage

By applying a reverse bias voltage, the maximum size of the depleted (charge carrier free) zone is limited. At some point the electric field will become so large that an electric *breakdown* will happen. This breakdown can have 2 sources, the *Zener* breakdown and the *avalanche* breakdown.
The Zener breakdown usually happens in highly doped semiconductors with a high reverse bias voltage applied. In such an np transition, the energy levels of the valence band electrons in the p-doped region roughly line up with the unoccupied states in the n-doped regions conduction band. The only thing preventing electrons from occupying the states in the conduction band, is a potential barrier which is triangularly shaped [20]. This barrier can be overcome by electrons utilizing tunneling effects. This tunneling probability φ is given by

$$\varphi \propto \exp\left(\frac{-4\sqrt{2m_e}E_G^{3/2}}{3e\hbar\mathcal{E}}\right). \tag{3.23}$$

As the electric field $\mathcal{E}$ across the junction grows large, the probability goes to 1. This means more and more electrons can tunnel through the energy gap. As more and more electrons reach the conduction band, the diode shows a Zener breakdown.
The avalanche breakdown on the other hand is based on multiplication processes. These multiplications take place, if the kinetic energy of conduction electrons, obtained from the electric field in the diode, is high enough to excite valence electrons in the conduction band through interactions. This new conduction electrons can also accumulate enough kinetic energy to promote even more electrons in the conduction band. This leads to an avalanche like production of charge carriers, the so called avalanche breakdown.

K-factor analysis

To quantify the avalanche breakdown behavior the following dimensionless function will be used [22].

$$K(I,V) = \frac{\Delta I}{\Delta V}\frac{V}{I} \tag{3.24}$$

, where $\frac{\Delta I}{\Delta V}$ is the slope of the IV-curve. The resulting K-factor can then be used to determine the breakdown voltage. For that a threshold value of the K-factor K_{bd} is utilized. The breakdown voltage V_{bd} is found as the voltage needed to achieve a $K > K_{bd}$. The threshold is determined empirically and individually for every chip.

3.4 Semiconductors as a particle detector

In semiconducting particle detectors the depleted region of a pn-junction serves as the detection volume. Incoming particles, that pass the charge carrier free zone, deposit energy in this zone by ionization, according to subsection 3.1. This energy deposition produces electron hole pairs in the depletion zone, of which the electrons are collected at an electrode. The number of electron hole pairs produced in this interaction is dependent on the energy loss of the traversing particle and the energy needed to produce the electron hole pairs. The latter one is bigger than the band gap in the silicon, as additional phonon excitations need to be taken into account. At room temperature this energy is $w_i = 3.65\,\mathrm{eV}$ [23]. The energy loss of particles is given by the asymmetric Landau distribution. In 300 µm silicon the mean value for minimal ionizing particles is $\langle \frac{\mathrm{d}E}{\mathrm{d}x} \rangle = 0.39\,\mathrm{keV\,\mu m^{-1}}$. This yields a charge of around 3.7 fC [17].
This collected charge can then be used to generate a signal in the readout part of such a detector. As the scope of this thesis only includes the active diode parts of silicon pixel detectors, the readout circuitry will not be explained in detail.
The exact geometry of a semiconductor detector can vary greatly, depending on its purpose. One common way, that will also be used in the MightyTracker, is the *pixel design*. Each pixel usually consists of one pn-junction that serves as detection volume. The pixel can also contain parts of the readout electronic. The readout system can then either be on a different chip which is then bonded to the pixel chip (hybrid pixel sensor) [17] like its shown in Figure 10. Another option is to include the readout electronic on the same chip as the sensitive part like its done in HV-MAPS [8]. As the proposed technology for the MightyTracker pixel detector is HV-MAPS, this will be discussed in more detail.

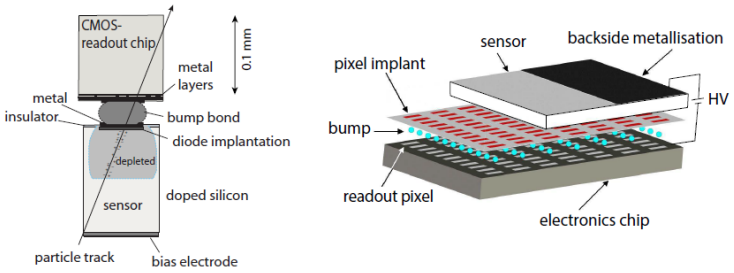

(a) Hybrid pixel cell.

(b) Pixel matrix.

Figure 10: (a) Schematic of a single pixel, with the analog part on the bottom and the digital part on top. (b) Layout of a whole hybrid pixel chip. [17]

3.4.1 HV-MAPS

High **V**oltage **M**onolithic **A**ctive **P**ixel **S**ensors are a type of monolithic silicon pixel sensor, which means that parts of the readout electronic are embedded in each pixel. HV-MAPS are produced in commercial HV-CMOS processes. These type of processes are typically used in the automotive industry [8].

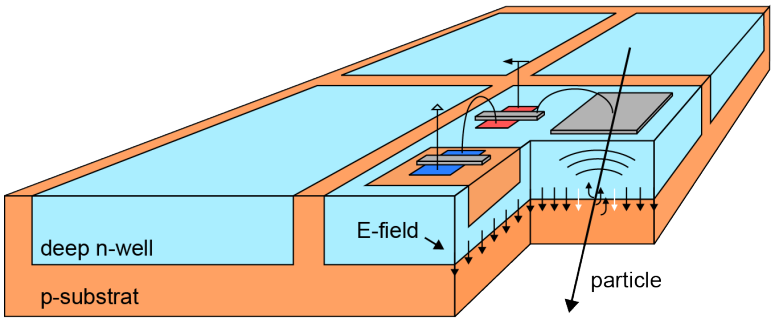

Figure 11: Schematic of a HV-MAPS chip with four pixels. [8]

Because of their monolithic structure, the material budget is very low compared to hybrid pixel sensors. This decreases multiple scattering of tracked particles. The high voltage allows for a great depletion volume. Each pixel consists of a deep n-well, which is embedded in the p-substrate. This n-well contains parts of the readout electronics like the amplifier. Additionally it serves as one part of the pn-junction. To control the shape of the electric fields within the pixels, additional guard ring structures are present (Figure 12). The high bias voltage can be applied either via a guardring or via the back directly at the p-substrate.

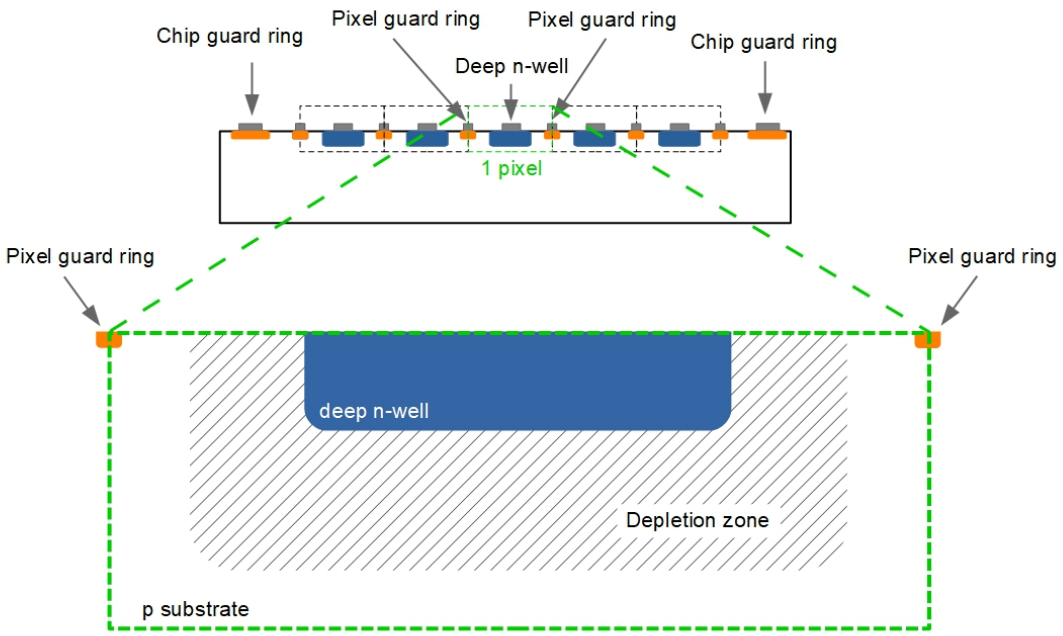

Figure 12: Schematic of an HV-MAPS guard ring structure. Adapted from [24].

3.5 Radiation Damage in semiconductors

As particle detectors are by design subject to high levels of radiation, the effects of radiation damage on the sensor design needs investigation. Radiation damage can be split into two components: damage to the substrate volume (e.g. silicon crystal structure) and surface damage, which mainly affects boundaries and the electronic readout circuits. [17]

The substrate damage is mainly caused by non ionizing energy loss (NIEL) by hadronic interactions of particles with the lattice atoms. This can one hand cause phonon excitations within the crystal, which will not damage the substrate by itself, but on the other hand it can also cause displacements or more complex distortions in the crystal structure. This has various effects on the leakage currents observed in the sensor. Furthermore, a change of the space charge can be caused, which changes the substrate and such the depletion and breakdown behavior. Additionally, space charges can be trapped by defects in the lattice structure. The influence of NIEL damage will not be further investigated within this thesis.

The second type of damage is typically produced by ionizing energy loss (IEL) of charged particles like protons, electrons or pions. The IEL can also do some damage in the bulk but to much less extent than the NIEL. IEL predominantly creates damage to the surface of silicon detectors. This surface damage mainly happens in silicon-dioxide (SiO_2) layers within transistors of the electronic circuits of the chip [25]. An ionizing particle traversing the SiO_2 will create e-h-pairs in it. Since the mobility of electrons and holes is quite different in SiO_2 ($\mu_e \approx 20\text{cm}^2/(\text{Vs})$, $\mu_h \approx 2 \times 10^{-5}\text{cm}^2/(\text{Vs})$ [26]), not all of these pairs can recombine. Some electrons

will be collected by positively biased anodes in the vicinity, while the holes remain in the SiO_2 and move slowly according to the electric field in the oxide. In the transition region between the oxide and silicon exist deep hole traps, in which the holes can be trapped. These trapped positive charges remain there and will affect the energy band structure on one hand but also the electric fields within the chip, which have an influence on the leakage currents of the chips.
IEL damage is also called TID (total ionizing dose) damage.

4 Experimental setups

In this section the different devices, programs and setups used within this thesis will be presented.

4.1 Investigated HV-MAPS

In this section the different HV-MAPS chips that were used to take data will be shortly introduced. All of those chips except the *BeBiPix* have been designed by Ivan Perić[1], while the BeBiPix was designed by Benjamin Weinläder[2].
These chips are designed for different purposes. While the MightyPix1 is designed as a prototype for the MightyTracker, the TelePix2 is designed to be used at the DESY test beam telescope. The BeBiPix was designed as a prototype that utilizes bipolar transistors in the readout electronic. As the different chips share many properties in their design, especially in the structure of the pn-transition region, it is expected that effects observed in one of those chips are equally present in other chips.
Table 1 shows some properties of the different HV-MAPS.

	TelePix2	MightyPix1	AtlasPix3.1	BeBiPix2	Run2020v1
Thickness [µm]	200	200	750	300	600
Chip size [mm^2]	20×13	5×20	20×21	1.2×1.3	5×4.8
Matrix Size	120×400	29×320	132×372	15×15	29×124
$V_{bd,Chip}$ [-V]	141	200	65 [3]	94	80 [4]
Pixel Size [µm^2]	165×25	165×50	150×50	40×40	165×25
$d_{N,Pix}$ [5] [µm]	9.0/6.5	14/11.5	15.66/15.1	7.8/7.8	9/6.5
N-well size [µm^2]	145×11.5	135×25.6	118.1×18.3	24×24	145×11.5
Resistivity [Ω cm]	370	370	370	50/20 [6]	370

Table 1: Overview over the used HV-MAPS chips

[1] Karlsruhe Institute of Technology (KIT)
[2] Physikalisches Institut (PI) Heidelberg
[3] Pixel and chip guard ring are shorted
[4] Pixel and chip guard ring are shorted
[5] Distance between N-well and pixel guard ring in the pixels in x/y
[6] Layer of 20 Ω cm on top.

4.2 Measurement setups

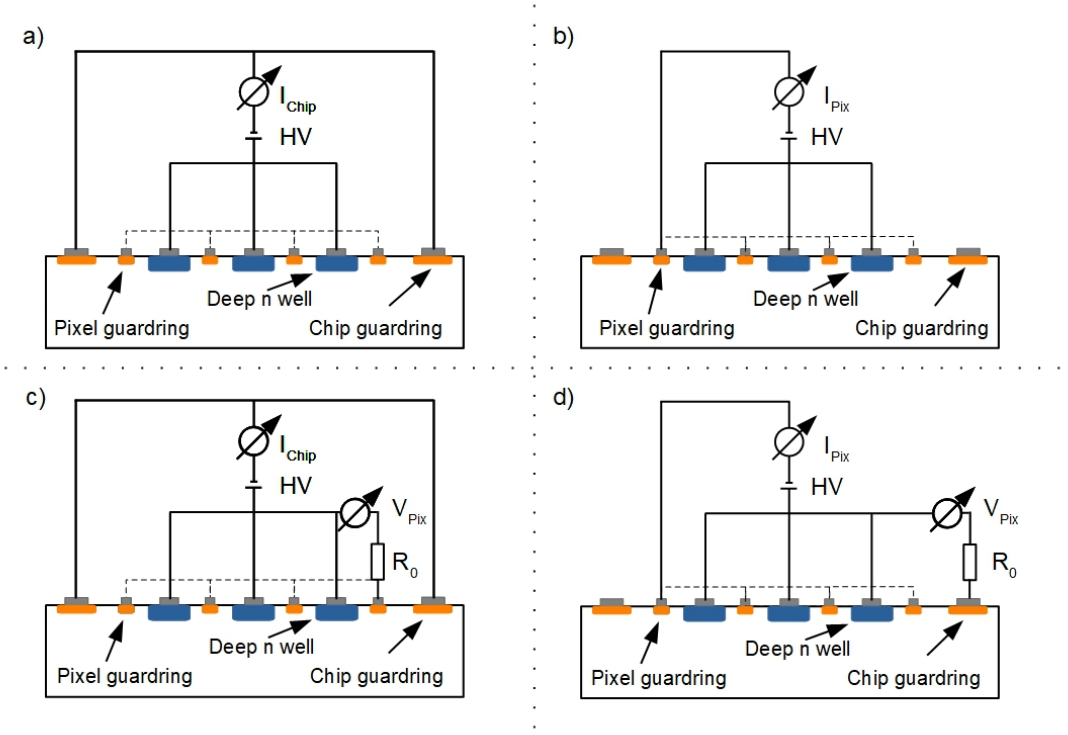

Figure 13: schematic of the circuitry of different measurement setups. a) Setup for IV curves with the high voltage applied at the chip guard ring. b) Setup for IV curves with the high voltage applied at the pixel guard ring. c) Setup for IV+V curves with the high voltage applied at the chip guard ring and an additional voltage measurement of the pixel guard ring voltage. d) Setup for IV+V curves with the high voltage applied at the pixel guard ring and an additional voltage measurement of the chip guard ring voltage. Adapted from [24]

Figure 13 shows sketches of the circuitry of the different measurement setups used. In this figure only 3 pixels are included, this is done for simplicity reason and does not represent reality. The resistor $R_0 = 10\text{G}\Omega$ was added as a voltage divider because the internal resistance of the voltmeter is too small, allowing current to flow through it, which affects the current measurement.
To apply high voltages and measure the resulting currents of different HV-MAPS a Keithley K2611b [27] power source measure unit (SMU) is used. It can apply voltages up to 200 V and measure currents with a resolution down to 100 fA depending on the range of the measurement. Additionally, it can be controlled and read out using a USB connection and a python script.
An additional Keithley K2000 multimeter [28] is used to be able to measure an additional voltage or a resistance. This can be used for example to measure the resistance of a temperature dependent resistor like a PT1000 to gain information on the chip temperature. The multimeter supports voltage measurements between 0.1 µV and 2000 V as well as resistance measurements between 100 µΩ and 120 MΩ. It is also easy to control remotely using the same interface as the SMU. To supply

the chips with low Voltage power, the Rhode&Schwarz NGE103b [29] as well as the Rhode&Schwarz Hameg HMP4040 [30] are used. The NGE103b supports up to 3 channels while providing up to 33.6 W per channel. The Hameg can supply 4 channels with a maximum power of 160 W per channel and a 384 W limit on all channels combined. Both feature an easy remote access to control and read out the supplied power.

4.3 Measurement Software

To perform all measurements within this thesis a dedicated measurement software has been developed. It can be used to measure IV curves. Furthermore it supports the parallel measurement of additional voltages or resistances. It can connect to, control and measure the HV power supply and supports the addition of a multimeter to measure an additional voltage or an additional resistance. It is also possible to connect to a LV power supply to collect data on the low voltage power consumption of a chip. To make the usage of the program user friendly a custom Graphical User Interface (GUI) was designed.

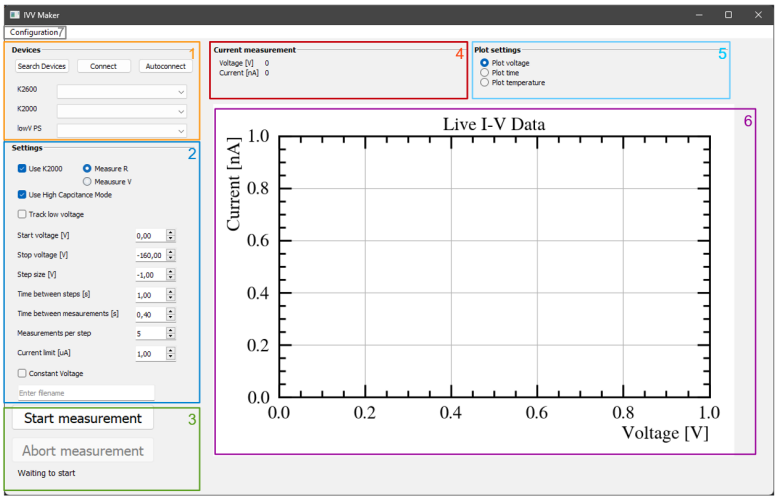

Figure 14: Graphical User Interface (GUI) of IVV Maker

The program features a section that handles the connected devices (Figure 14). It allows to search for (either via USB or Ethernet) connected devices and will add them to drop down menus where you can select the desired devices. It also features an auto-connect function that combines the search and select process.
In the next part of the GUI, are the settings for the measurements. For IV measurements it is possible to set the voltage for the start of the sweep as well as the stop voltage. Additionally, it is possible change the stepsize, the number of measurements per step and the time between measurements. To prevent charge up effects influencing the current measurement while increasing the voltage, it is also possible to set a time delay between increasing the voltage and taking the first measurement at the new voltage step. As in some cases it is also needed to apply a constant voltage and monitor the current while e.g. irradiating the chip, there is also the option to run at a constant voltage. To additional track a second voltage, a

resistance or the outputs of another (low voltage) power supply, there are options to enable/disable them as needed.
The third section contains the start and abort measurement buttons. In the remaining UI there are the latest measurements, and a plot where the collected data is plotted in real time. The online monitoring can plot the current against the voltage, the time and the temperature, if the resistance of a PT1000 is read out.

4.4 Cooling Setups

To study the diode characteristics of silicon pixel detectors at changing temperatures, two different cooling setups were used The first one being an ELCOLD laboratory freezer [31]. This freezer is able to cool down to $-50°C$, but not to hold the temperature stable for a longer period of time. Therefore it's only used to measure the current while cooling down or warming up the chip. To take IV curves at different temperatures a Binder climate chamber [32] is used. This has the advantage, that a much more stable temperature can be achieved, while also being able to control the humidity.

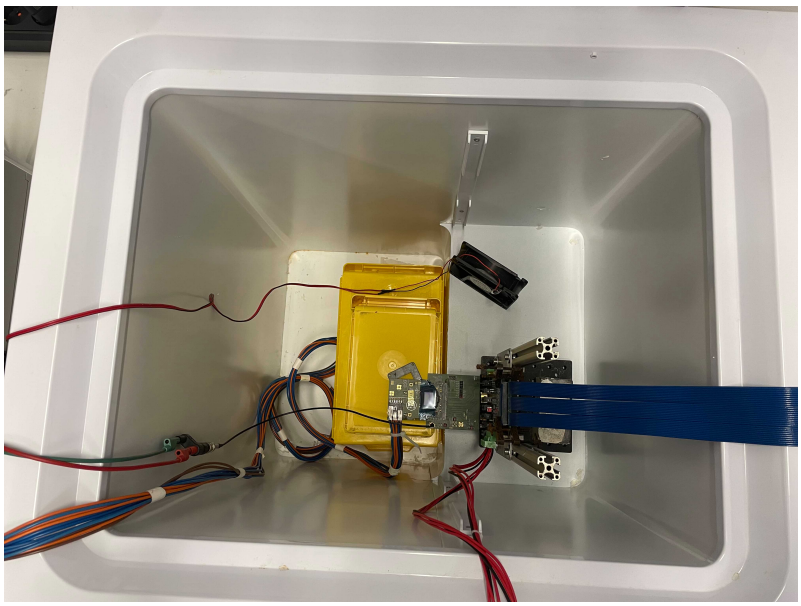

Figure 15: Cooling setup in the freezer.

4.5 X-Ray Irradiation Setup

To study the effect of IEL/TID irradiation on the chips, a Phywe XR4.0 [33] X-ray tube in combination with a tungsten anode was used. It features a maximum acceleration voltage of 35 kV, which was used for all irradiations. The X-ray current can be adjusted between 0.01 mA and 1.00 mA in steps of 0.01 mA. Figure 16 shows a chip being irradiated in the X-ray tube.

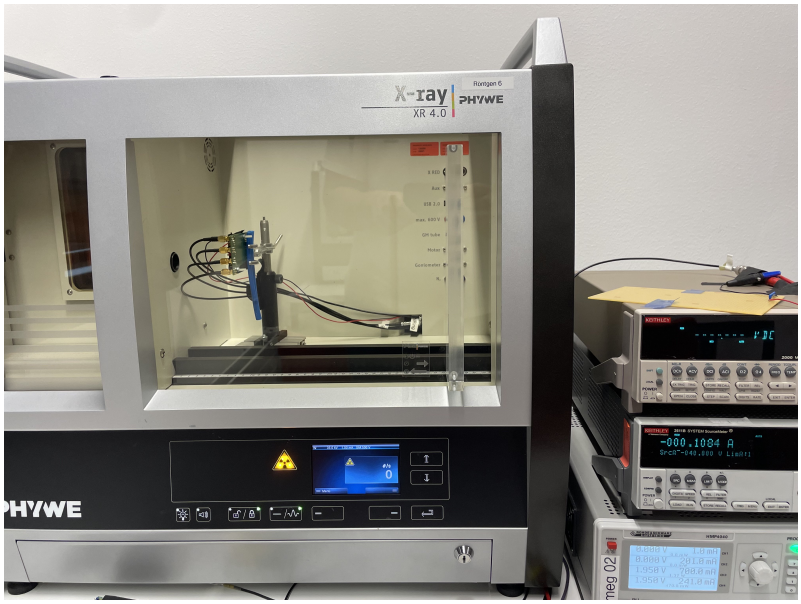

Figure 16: XRay irradiation setup.

A typical energy spectrum of a tungsten anode is shown in Figure 17. Note that the spectrum shown only features energies up to 28 keV, while the maximum energy featured in the used tube is 35 keV

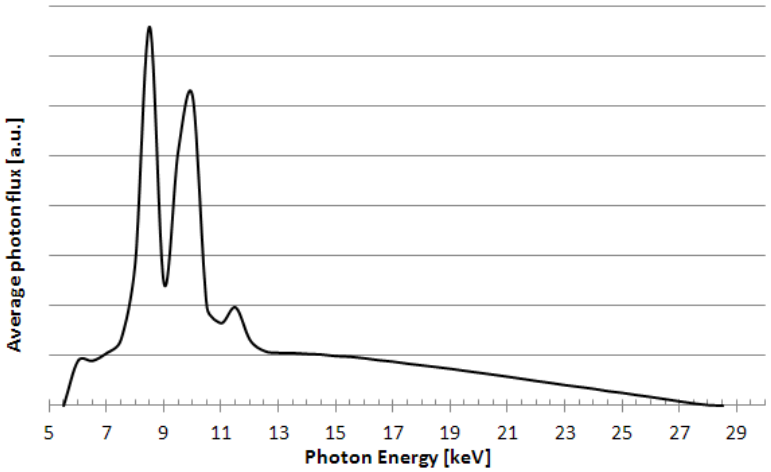

Figure 17: X-ray spectrum of a tungsten anode. The spectrum features 2 distinct peaks, as well as a continous Bremsstrahlung spectrum up to the X-ray voltage of 28 kV. [34]

5 IV Characteristics

In this first part the diode structure of different chips are studied using the IV characteristics. It is expected that chips, which share similar properties, especially pixel size and wafer resistivity and production process, also share properties in their respective IV curves.
All IV characteristics that will be presented in this section have been measured using the setup described in the previous section. For all measurements unless stated otherwise the starting voltage was set to 0 V and the stepsize to −1 V. The stop voltage was set depending on the measured chip, as there is no point of further increasing the voltage after the breakdown. To prevent damaging the chips with high currents, the current limit of the source measure unit is set according to the maximum expected current (which was tested beforehand). There are 5 current measurements taken at each voltage step. The error of the current measurements is purely based on the statistical error of those 5 measurements. The systematical error of the current measurement is hard to estimate reliably, as for one the resolution of the source measure unit changes depending on the current limit and on the other hand all wires and connectors used to get the voltage to the chip have an influence which is nearly impossible to estimate reliably. Additionally the high capacitance mode of the source measure unit is used, which is specifically designed to be used for diodes and other semiconducting elements. To prevent any build up charge to alter the current measurement, there is a delay of 1 s added between applying a new voltage and taking the first current measurement at this step.
As discussed in subsection 3.3 the following relation between the measured current I and the applied voltage V is expected:

$$I \propto \sqrt{V}. \tag{5.1}$$

While increasing the voltage, at some point the avalanche breakdown of the diode is expected, as the kinetic energy of the electrons increases with the increased voltage. An example for such an IV curve of a TelePix2 with the high voltage applied at the chip guard ring is shown in Figure 18. The plot shows the measured leakage current against the bias voltage. It can be split into 3 regions, with the first one the depletion region, where the IV curve obeys the relation (5.1). The second region that is observed in the IV curves of different chips is the so called transition region, where neither (5.1) nor breakdown behavior can be observed. The third region is the avalanche breakdown, that is discussed in subsection 3.3.

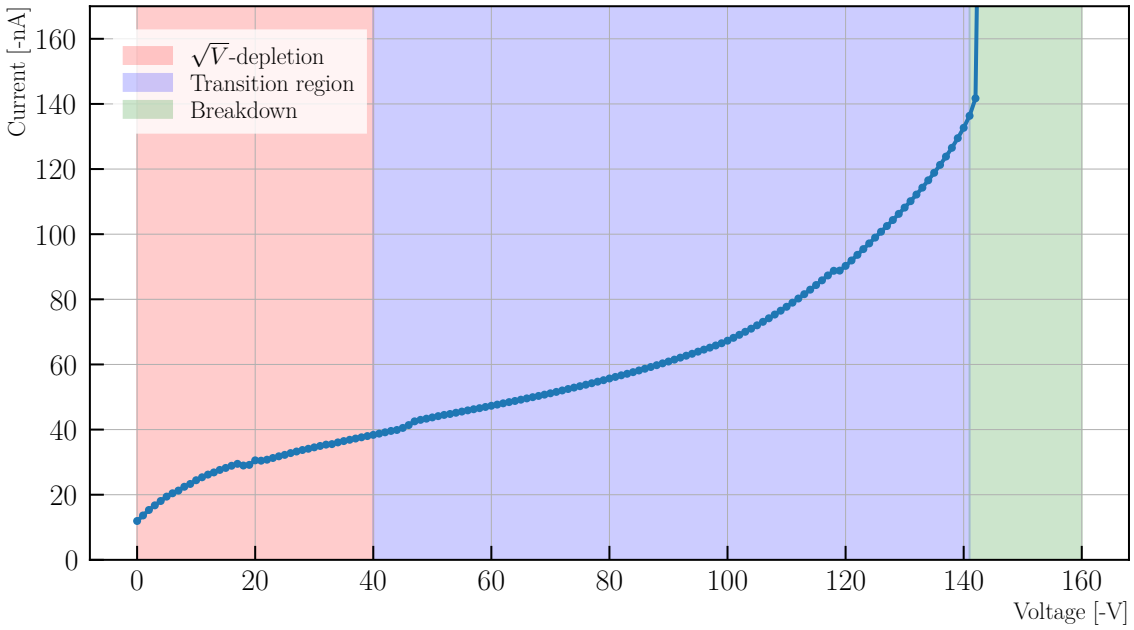

Figure 18: IV curve of a TelePix2, HV applied at the Chip Guard Ring.

5.1 Depletion region

First the depletion region where relation (5.1) holds true will be investigated. This is present in the IV curves of most[7] chips that have been examined within this thesis. In Figure 19 IV curves for a MightyPix, TelePix2 and AtlasPix3.1 are shown. In all three of the curves the $\sqrt{V}$ behavior can be observed. In this particular representation it can be recognized by the linear part of the plots. Also the two other regions, the transition region and the breakdown, can be observed. The different breakdown voltages can be explained by different pixel sizes and is done in the next subsection.

[7]except the BeBiPix

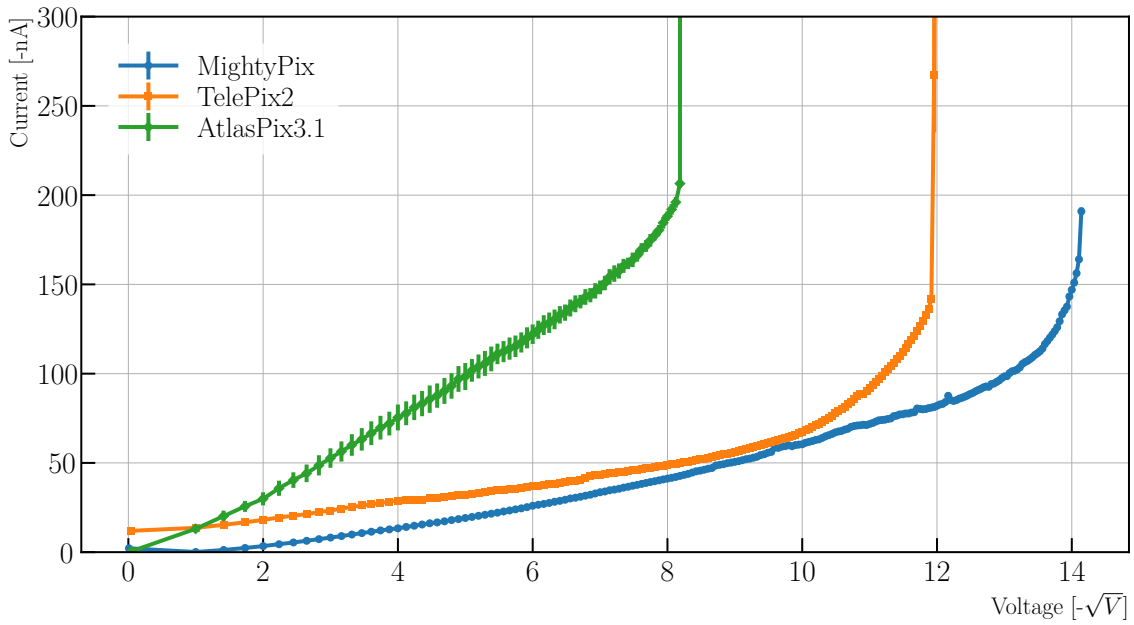

Figure 19: IV curve of a MightyPix, TelePix2 and AtlasPix3.1, current plotted against $\sqrt{V}$, HV applied at the chip guard ring.

To further investigate this behavior, a fit function of the form $I(V) = a\sqrt{V} + I_0$, with a scaling factor a and a constant offset I_0 will be fitted on the data. This is only be shown for the TelePix2 as an example
For the fit only the data from 0 to $V_{T,Chip} = -45\,\mathrm{V}$ (obtained from the fit insubsection 5.3) will be taken into account, as above this voltage the transition region starts.

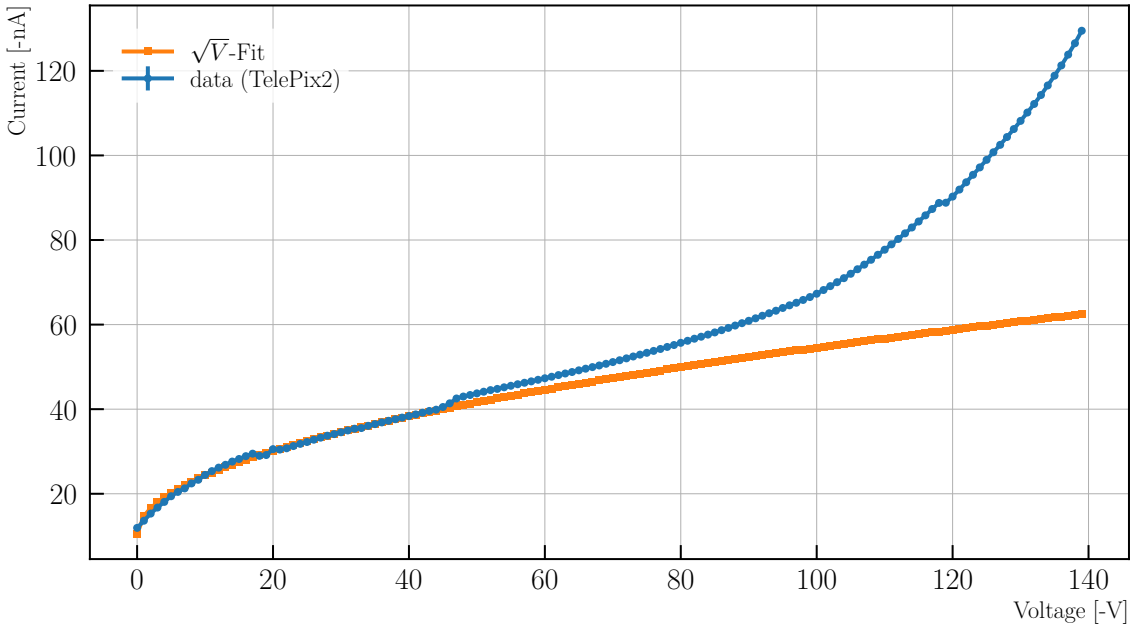

Figure 20: $\sqrt{V}$-fit on the IV curve of a TelePix2, HV applied at the chip guard ring.

Visually this fit seems to describe the data very well up to an applied voltage of

around $-45\,\mathrm{V}$. Similar results can be obtained by using data of the other chips except the BeBiPix, which will be discussed in more detail later. At $0\,\mathrm{V}$ the fit seems also to not describe the data, but as the chip will never be operated without applying a bias voltage, the leakage current at $0\,\mathrm{V}$ is not further investigated. The ability to fit a simple $\sqrt{V}$ on the data again strongly indicates that the IV characteristic, at least until a certain threshold voltage, in fact obeys the relation (5.1). This means that the complex chip structure can successfully approximated by a simple pn-transition. Until now this behavior was only shown for measurements where the high voltage was applied at the chip guard ring. the fit can also performed on data taken with high voltage applied at the pixel guard ring (see Figure 21). For this the start of the transition region is found to be $V_{T,Pix} = -38\,\mathrm{V}$. The relation between $V_{T,Chip}$ and $V_{T,Pix}$ will be discussed in subsection 5.3.

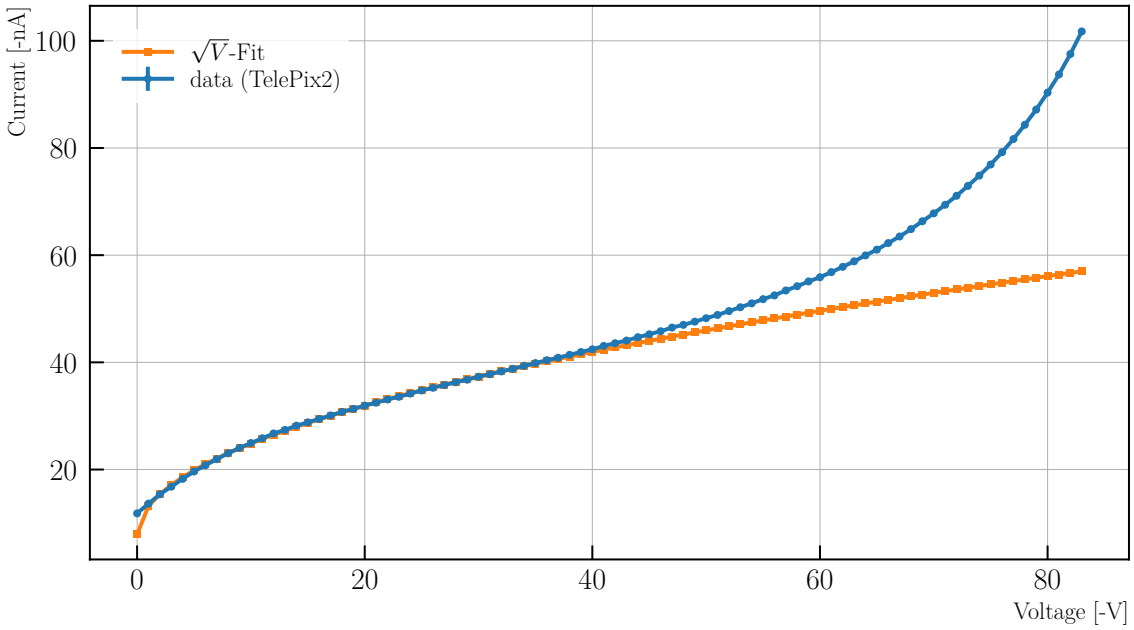

Figure 21: $\sqrt{V}$-fit on the IV curve of a TelePix2, HV applied at the pixel guard ring.

5.2 Breakdown

The next part of the IV characteristic, that will be investigated, is the breakdown. As mentioned earlier, the breakdown in HV-MAPS is based on the avalanche breakdown. At high enough electric fields produced by the applied HV, the electrons in the conduction band have enough kinetic energy to promote more electrons from the valence to the conduction band. This leads to an avalanche of conducting electrons, which is called avalanche breakdown. The breakdown voltage is dependent on the internal structure of the different chips, as the strength and structure of the electric field depends on the exact geometry of the pixels.
The breakdown voltage of a HV-MAPS chip is an important quantity as it determines the maximum bias voltage for a chip. This maximal bias voltage determines the biggest possible size of the depleted (= detection) volume.
In this section different chips and bias schemes are investigated regarding the breakdown voltage. To do this, the exact behavior of the IV curve close to the breakdown voltage needs to be analyzed, which is done by utilizing the K-factor analysis (sub-

section 3.3). Again, this first general analysis of the breakdown is done on data of the TelePix2 exemplary, but the same methods will be used analyzing the other chips. The K-factor threshold K_{bd} is chosen individually for each chip. It should be high enough to not predict a breakdown for small fluctuations, but also not to high to prevent overestimating the breakdown voltage. The exact value of it is chosen arbitrarily based on fluctuations within the IV curves of a chip. For the TelePix2 as well as the MightyPix a threshold of 5 was determined.
The K-factor analysis of the IV curve of the TelePix2 (TP2) is shown in Figure 22. With this the breakdown voltage $V_{bd,\text{Chip}} = 141\text{V}$ can be determined. All breakdown voltages that are mentioned within this thesis are determined using this method.

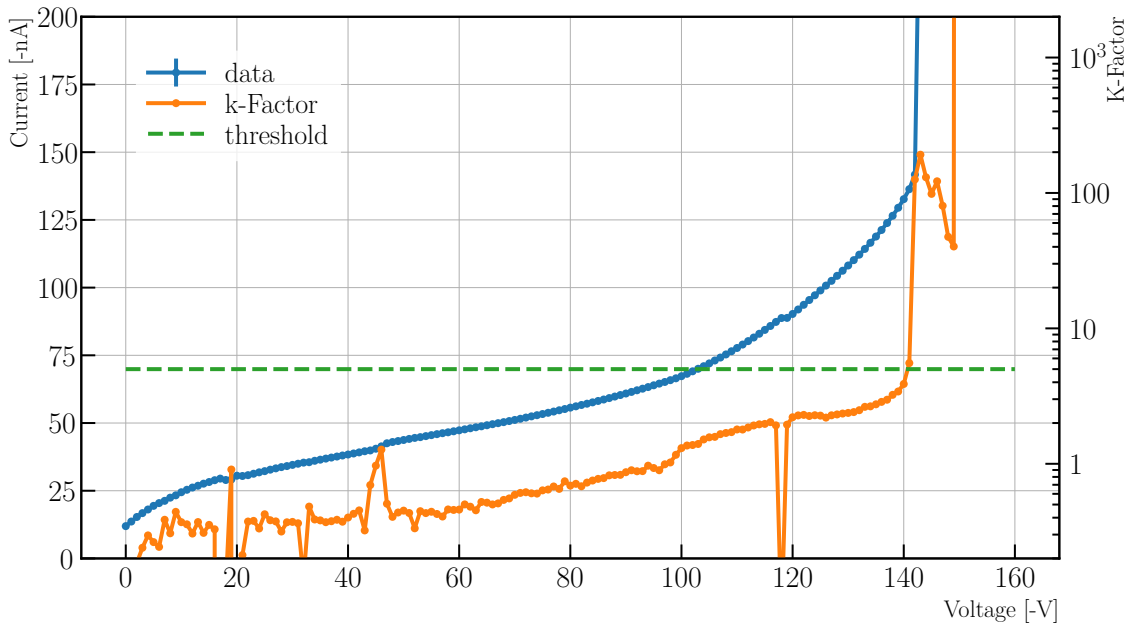

Figure 22: K-factor analysis of a TelePix2 IV curve (HV applied at the chip guard ring). The threshold of 5 is plotted as the dashed green line.

In the plot there are some fluctuations observed, especially at around $-118\,\text{V}$ there seems to be a little jump in the current. A possible reason is a voltage drop/spike in the $230\,\text{V}$ network which is powering the high voltage supply. This leads to instabilities in the current measurement which can cause jumps like that.
In a next step the breakdown voltage will be determined while applying the bias voltage at the pixel guard ring. The IV curve of a chip guard ring biased TelePix2 is shown in Figure 23. With the same method as before, the breakdown voltage can now be determined to be $V_{bd,\text{Pix}} = 85\,\text{V}$

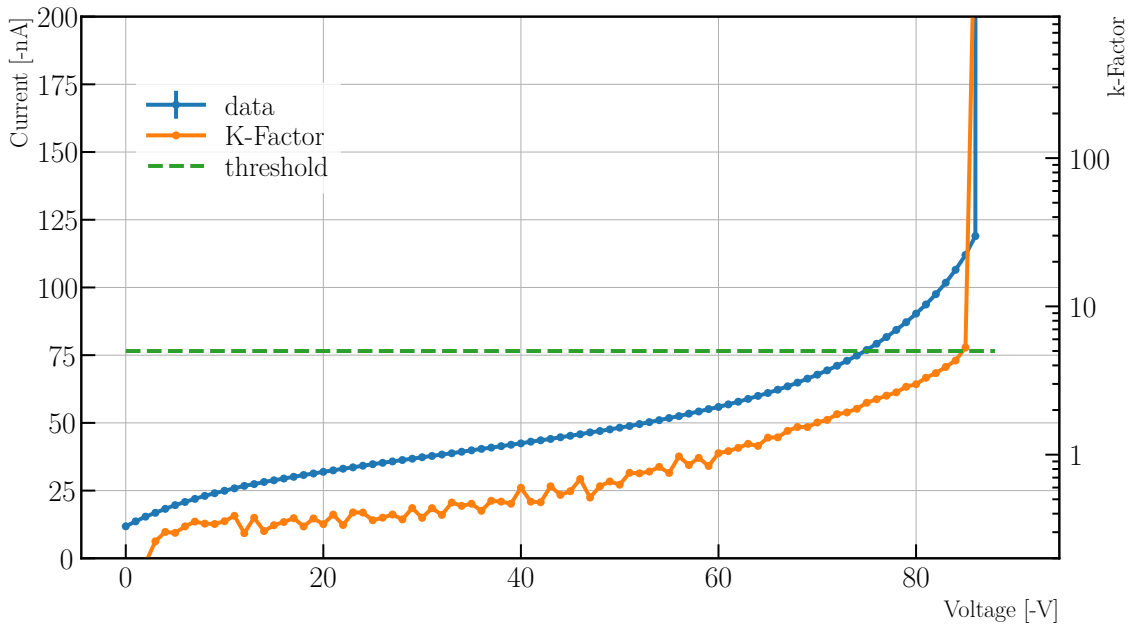

Figure 23: K-factor analysis of a TelePix2 IV curve (HV applied at the pixel guard ring). The threshold of 5 is plotted as the dashed green line.

The breakdown voltage of a pixel guard ring biased TelePix2 is quite a bit lower than that of a chip guard ring biased one. To further evaluate the origin of the breakdown it is very interesting to look at the so called VV-curve. The measurement setup described in section 4 allows to measure an additional voltage while taking data for the IV curve. This enables the option to measure the voltage at the pixel guard ring as a function of the bias voltage applied at the chip guard ring. The results of this measurement are shown in Figure 24.

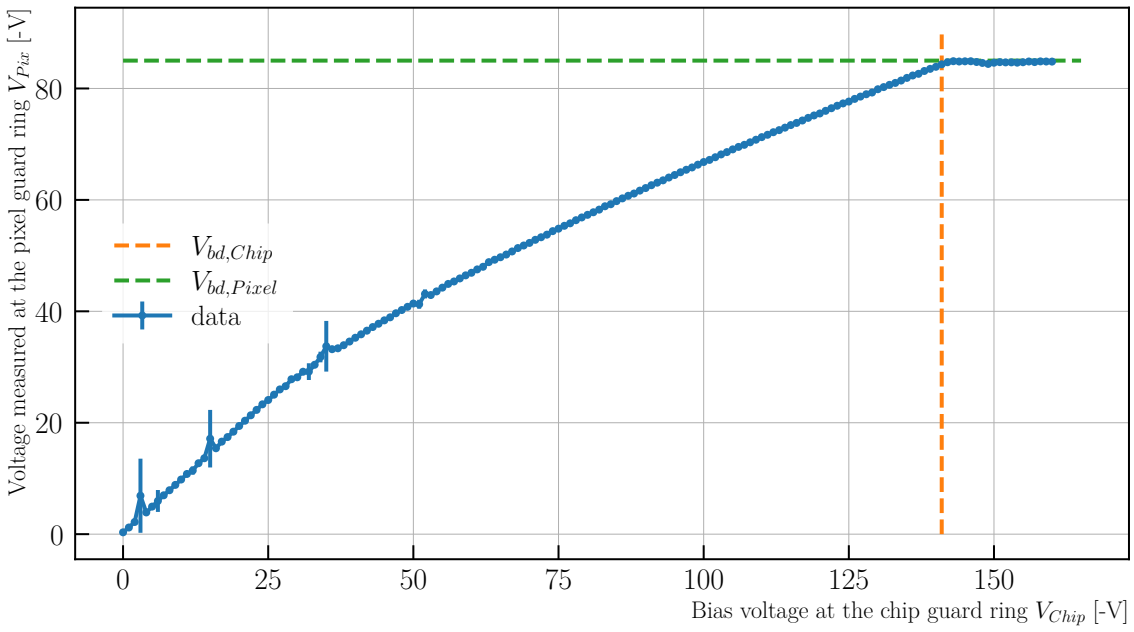

Figure 24: VV curve of a TelePix2, the dashed orange and green lines represent $V_{bd,\mathrm{Chip}}$, $V_{bd,\mathrm{Pix}}$ respectively.

This plot indicates that the breakdown happens inside the pixel, if the potential difference between the deep n-well (which is at 0V) and the pixel guard ring exceeds −85 V regardless of where the voltage is applied. This was also observed in other chips not examined within this thesis [35].
Within the VV-measurement it is also observed that the voltage measured at the pixel guard ring stays constant for bias voltages $> V_{bd,Chip}$. The cause for this behavior is not clear.
The observations made in the presented measurements leads to the conclusion, that the breakdown happens between the pixel guard ring and the n-well in each pixel. This suggests, that the exact value of the breakdown voltage is dependent on the distance d_{N-Pix} between those two structures. The breakdown voltages of the other chips are presented in Table 2.

Chip	$V_{bd,\text{Chip}}$ [V]	$V_{bd,\text{Pix}}$ [V]
TelePix2	141	85
MightyPix	200	120
AtlasPix3.1	65	- [8]
Run2020[9]	83	83
BeBiPix [10]	94	84

Table 2: Breakdown voltages of the different chips used within this thesis.

To deeper analyze the dependence of the breakdown voltage on the internal structure of the HV-MAPS chips, the breakdown voltage at the pixel guard ring is plotted against the distance between the deep N well and the pixel guard ring. This is only done for the TelePix2, MightyPix and Run2020v1 chip, as these are all produced by the same manufacturer and utilize a similar wafer resistivity. From (3.20) a quadratic dependence of the breakdown voltage on the distance is expected. As only 3 points are plotted, with the Run2020v1 and TelePix2 utilizing the same deep N well - pixel guard ring distance, this relation can not be tested to full extent on this data set. However certain trends can be observed in this plot. The TelePix2 and Run2020v1 chip have a very similar internal structure, which leads to a very similar breakdown voltage between them. The MightyPix utilizes a higher distance between deep N well and pixel guard ring which leads to a higher breakdown voltage, which is what is expected.

[8] Pixel guard ring not contacted
[9] pixel and chip guard ring are shorted
[10] With floating N guard ring

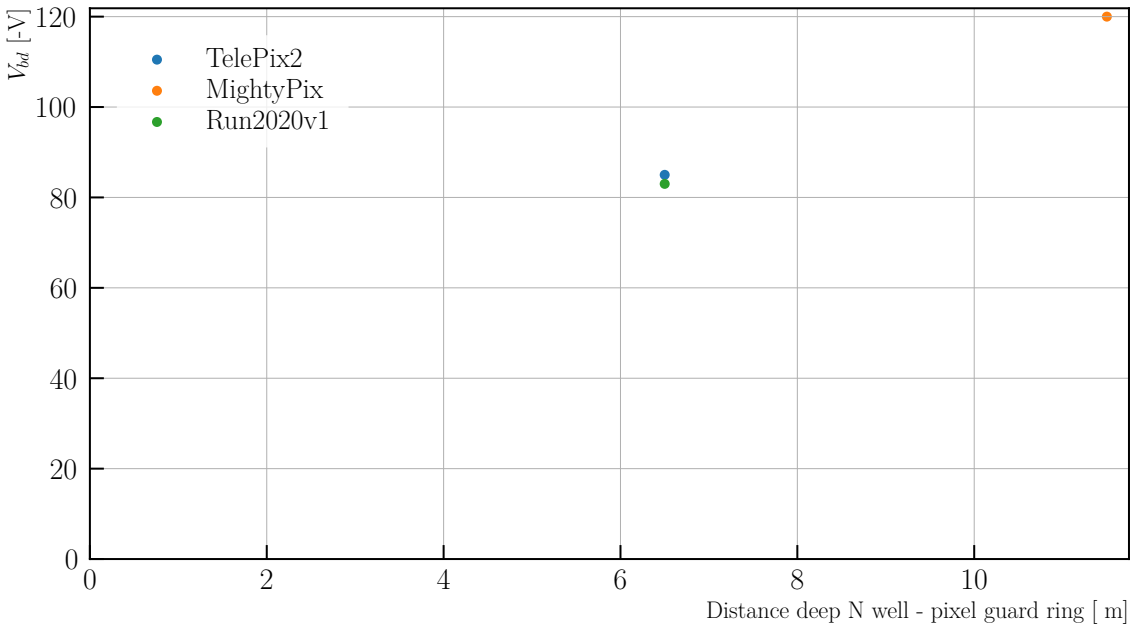

Figure 25: Breakdown voltage plotted against the deep N well - pixel guard ring distance.

An even deeper analysis of (3.20) would be possible by investigating more diverse HV-MAPS chips with different internal structures and possibly also a different resistivity. However this is not done within this thesis.

5.2.1 Influence of an additional N guard ring

The BeBiPix features an additional n doped guard ring between the chip guard ring and the pixel matrix called **N guard ring**. This is also the case for other chips (for example in the MightyPix), but while in the other chips this N ring is just floating, in the BeBiPix it is possible to apply or measure a voltage V_N at this ring. A schematic of the guardring structure of the BeBiPix is shown in Figure 26.

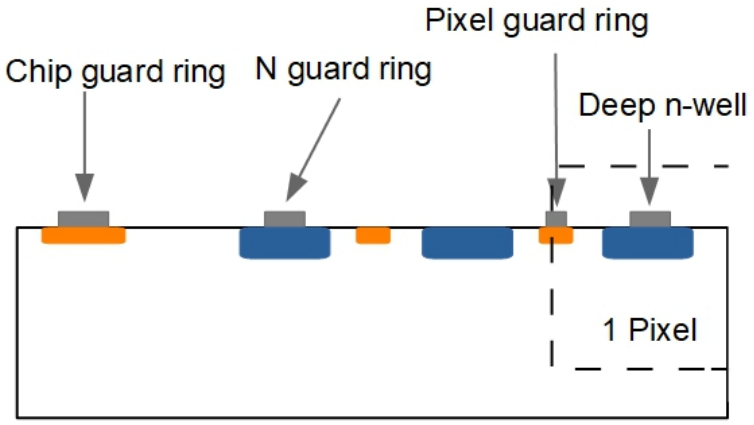

Figure 26: Schematic of the guard ring structure of the BeBiPix

V_N [V]	V_{bd} [V]
-4	-89
-2	-87
0	-84
2	-81
float	-83

Table 3: Breakdown voltages of the BeBiPix for different potentials of the additional N guard ring.

It has to be mentioned that no region that follows a $\sqrt{V}$ behavior is observed in the IV characteristic of BeBiPix. There are some ideas on why this is the case. The BeBiPix was produced by a different manufacturer using a different process. Additionally the chip is very small and has far less pixels than any of the other chips. It is possible, that the observed leakage current originates not only in the diodes of the pixels, but has other origins like the additional epi layer on top of the pixel matrix.
Nevertheless a breakdown is also found for this chip using the K-factor analysis. The influence of the N guard ring voltage on the breakdown voltage observed here, is predicted to appear in other chips as well.
In Figure 27 the IV curves for different applied N guard ring bias are shown. The breakdown, which manifests itself in the plot as the sudden increase in the current, is shifted to higher/lower voltages $V_{bd,N}$ depending on the voltage V_N applied at the N guard ring. The resulting shifts are shown in Table 3. With this data it is suspected that the breakdown voltage is shifted with the potential that is applied at the N guard ring. As the resolution of the measurements is only 1 V, the accuracy of this prediction is not too high. IV measurements with a higher resolution in the breakdown region are needed to investigate this deeper.

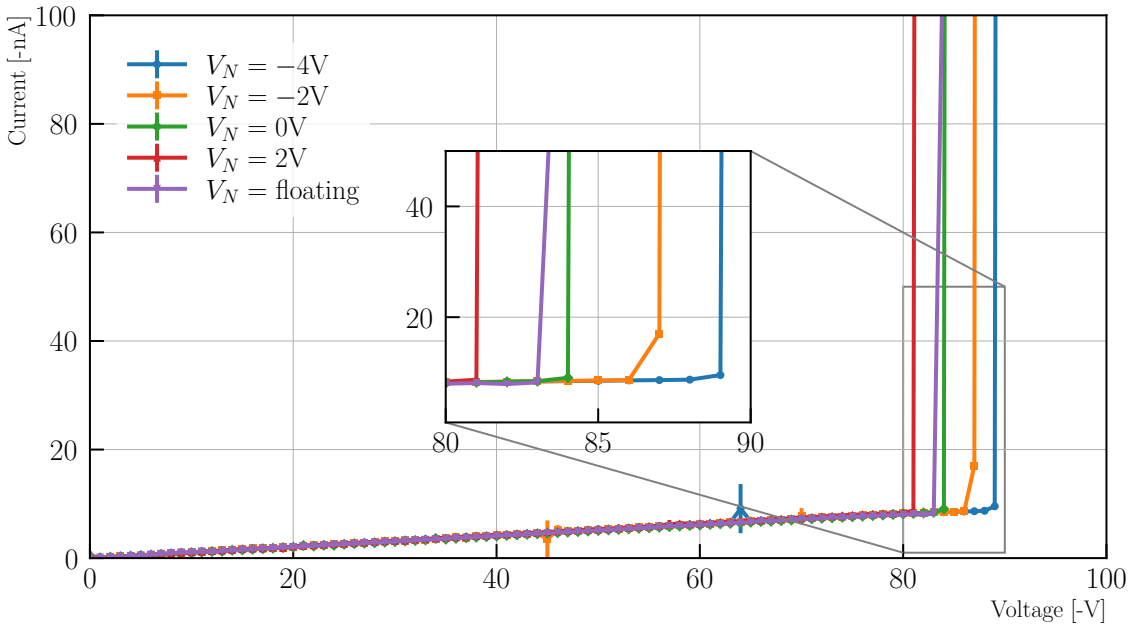

Figure 27: Influence of V_N on the breakdown voltage of the BeBiPix

5.3 Transition Region

As stated earlier, the $\sqrt{V}$ description of the IV curves only holds up until certain voltages, depending on chip and biasing. However no breakdown is observed in the region that follows. It is suspected that *trap assisted tunneling* (TAT)[36, 37] is responsible for this deviation.
The TelePix2 with chip guard ring biasing will again be used as a reference to investigate this region. Its IV curve including the $\sqrt{V}$ fit was already shown in Figure 20. To describe the IV curve in the transition region, a correction for TAT must be made. With this correction the leakage current is described by:

$$I(V) \propto (1 + \Gamma)\sqrt{V} \tag{5.2}$$

with the correction $\Gamma \approx \frac{\mathcal{E}_{eff}}{(k_B T)^{3/2}} \exp\left(\frac{\mathcal{E}_{eff}}{(k_B T)^{3/2}}\right)^2$, which accounts for the TAT. $\mathcal{E}_{eff}$ is the effective field strength of the electric field, which in a good approximation fulfills $\mathcal{E}_{eff} \propto V$. This makes it possible to obtain a fit function that should describes the IV curve in the depletion and the transition region. For that one more assumption needs to be made. As TAT is only expected for electric fields of the order $1 \times 10^5\,\mathrm{V\,cm^{-1}}$, a Θ-function (Heavyside function[11]) is used to account for this. It should however be noted that the electric field strength varies greatly inside the pixel. With the Θ-function a cut where the leakage current resulting from TAT becomes significant is assumed. This cut is called V_T. The resulting function that is used to describe the data is:

$$I(V) = I_0 + a\sqrt{V} + b\Theta(V - V_T)V^{3/2} \exp(cV)^2 \tag{5.3}$$

, where again I_0, a, b, c are used as a constant offset in the current and scaling factors respectively. This function is fitted to the IV curves of the TelePix2 presented earlier. In Figure 28 the bias voltage is applied at the chip guard ring, while the data shown in Figure 29 is obtained with a pixel guard ring biased TelePix2.
Visually the fit seems to describe the data very well. Also the residuals, plotted below as the deviation between the fit and the actual data show a great compatibility. Some features in the data lead to some deviations though. Especially the small jumps at around 20, 45 and 120 V produce bigger deviations. It is suspected that these jumps are the result of a voltage drop at the 230 V supply network, with which the HV source meter is powered. These voltage drops are the result of power hungry devices in the same circuit turning on/off. The source meter is not able to compensate these effects instantly, which leads to systematic errors in the current measurement. Nevertheless the TAT part of the leakage current is able to explain the deviation of the IV curve from the $\sqrt{V}$ dependency. For the transition voltage with chip guard ring basing a value of $V_{T,Chip} = -45\,\mathrm{V}$ is obtained from the fit.
It is suspected that this is an effect in the silicon bulk itself. A significant indication for that is, that the same fit function is able to accurately describe the data of an IV measurement, where the HV bias voltage was applied at the pixel guard ring (see Figure 29). Here a transition voltage of $V_{T,Pix} = -38\,\mathrm{V}$ was determined from the fit. The transition voltages V_T that are found for the chip/pixel guard ring respectively, are well compatible with the VV-curve as shown in Figure 30.

[11] $\Theta(x) = \begin{cases} 1 & \text{for x} \geq 0 \\ 0 & \text{for x} < 0 \end{cases}$

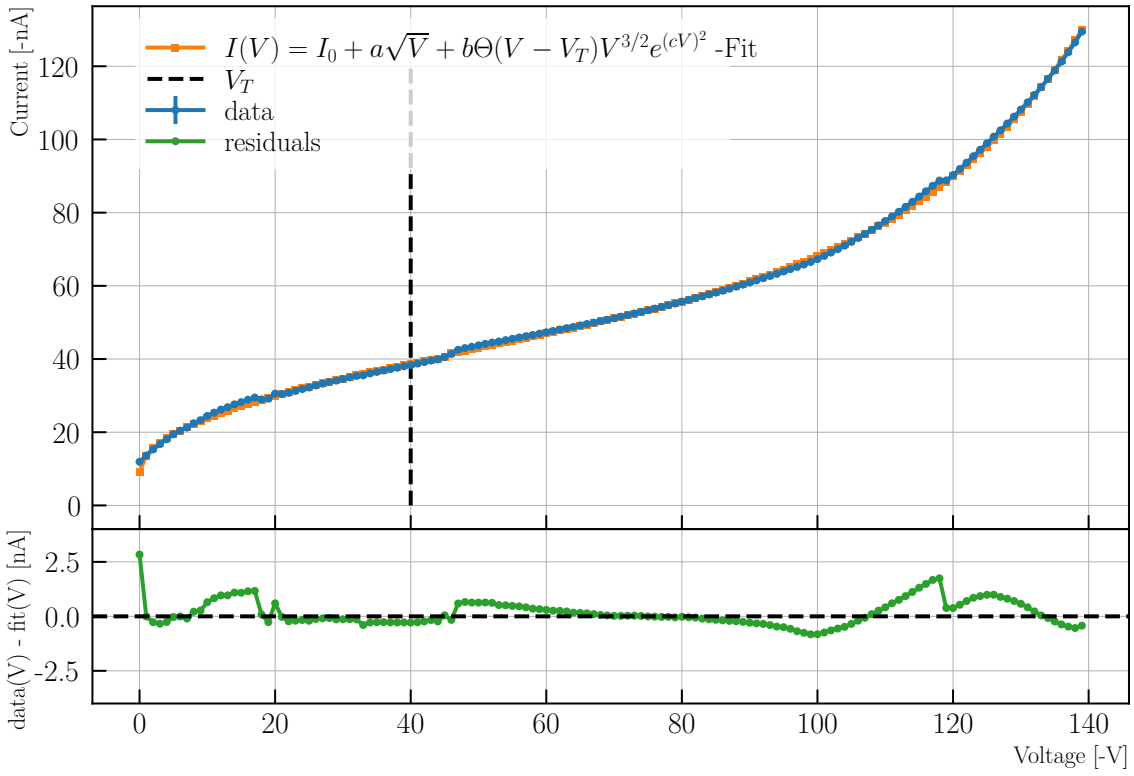

Figure 28: Fit of the IV curve of a chip guard biased TelePix2 using $I(V)$ to fit the data. At the bottom the residuals ($I_{meas} - I_{fit}$) of the plot are shown.

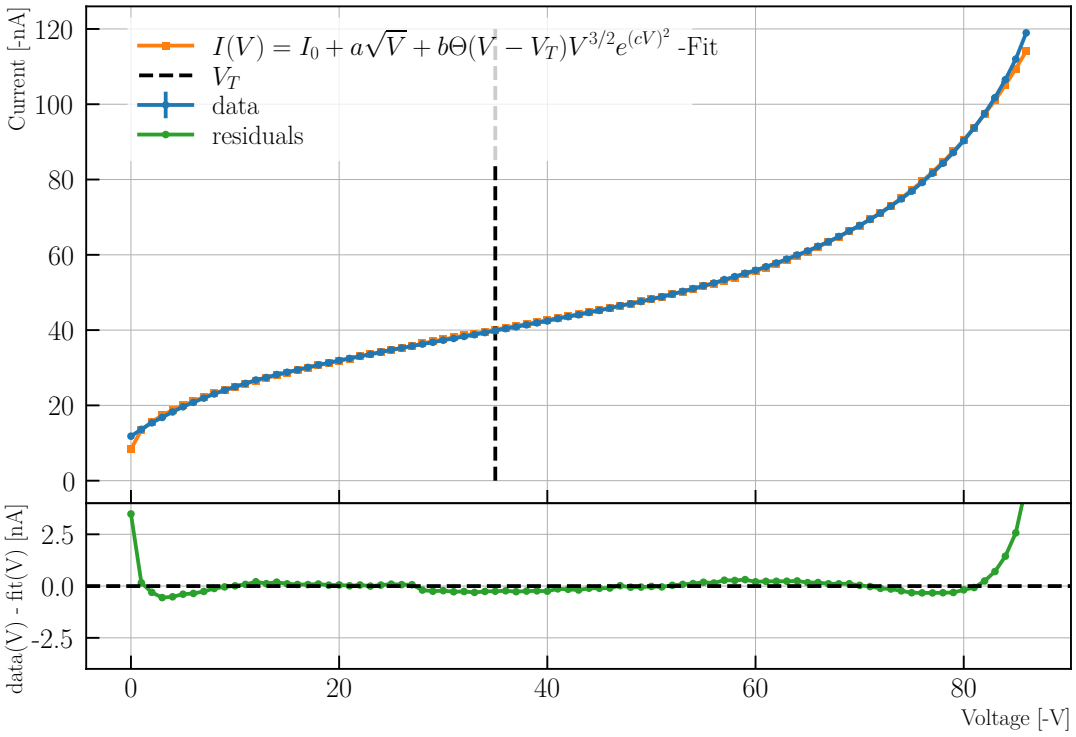

Figure 29: Fit of the IV curve of a pixel guard biased TelePix2 using $I(V)$ to fit the data. At the bottom the residuals ($I_{meas} - I_{fit}$) of the plot are shown.

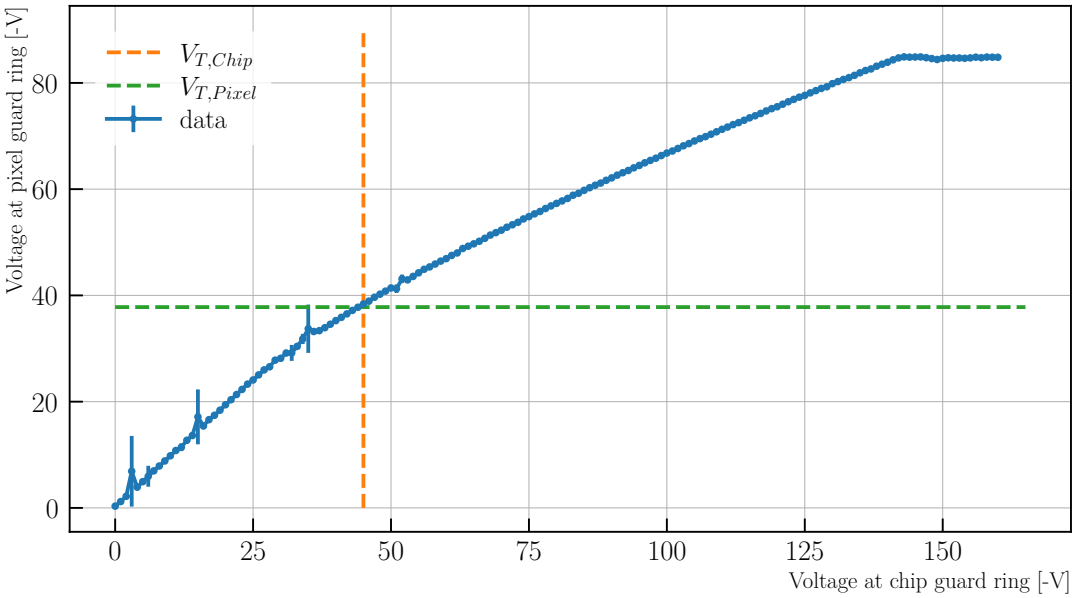

Figure 30: VV-curve of a TelePix2. The transition voltages for the chip and pixel guard ring biasing respectively are shown.

In this section it is shown that the approximation of a HV-MAPS as a simple diode regarding the leakage current is valid. For even more accurate description of the leakage currents in HV-MAPS an extensive simulation of the electric fields and their effects on the leakage current is needed.

6 Temperature Effects on the IV Characteristic

Temperature changes have a big impact on the leakage currents observed in HV-MAPS. For the operation of such a chip a fixed temperature must be chosen depending on various external and internal factors like available cooling, power consumption of the chip and the influence on the operation. To evaluate the influence on the operation of the chip, the leakage current is an important characterization.
This section investigates two different aspects of this temperature dependence. In the first part the influence of temperature changes on the breakdown voltage is discussed, while the second part focuses on the temperature dependence of the leakage current itself.

6.1 Breakdown voltage at different temperatures

The measurements for the shift of the breakdown voltage are performed in the climate chamber. The climate chamber allows for a control of the humidity, which at that time worked at temperatures above 0 °C, while for lower temperatures the climate chamber has problems controlling the humidity. The temperature dependence of the breakdown is measured using the TelePix2 and a simple diode as a crosscheck. Measurements are performed at five different temperatures between 0 °C and 40 °C. They are shown in Figure 31 and Figure 32 for the diode and TelePix2 respectively.

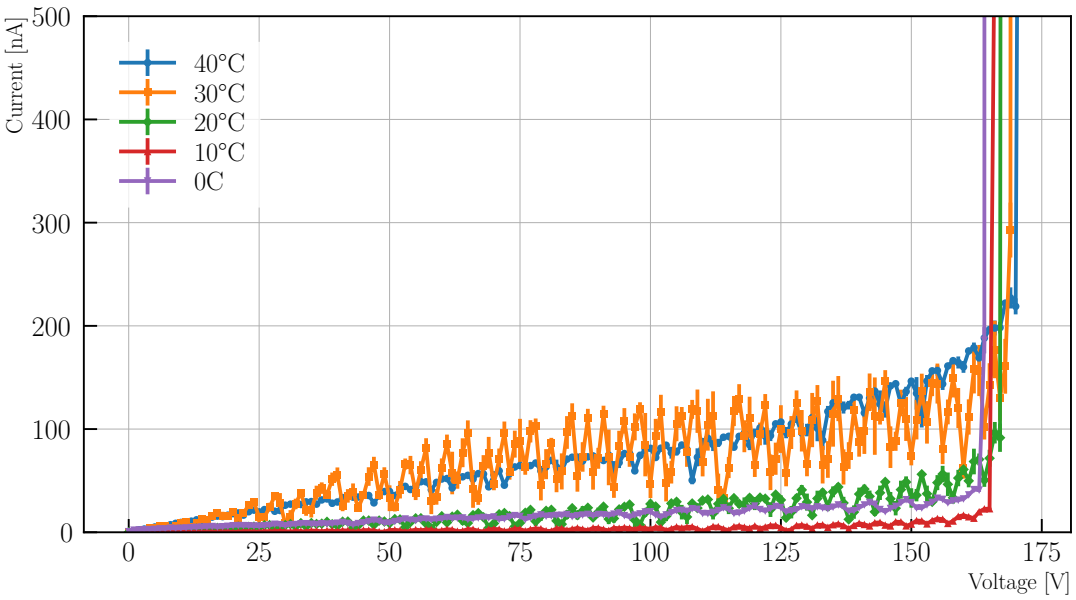

Figure 31: IV curves of a diode at different temperatures ranging from 0°C to 40°C

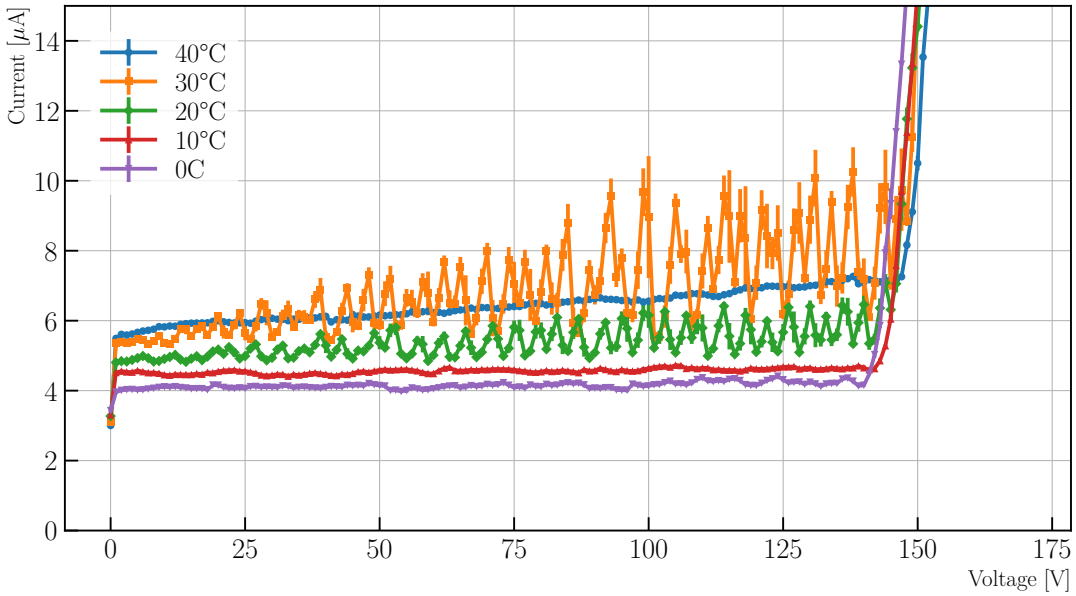

Figure 32: IV curves of a TelePix2 at different temperatures ranging from 0°C to 40°C

The big fluctuations in the IV curves at 30 °C and to some extent at 20 °C are probably caused by the climate chamber turning off/on a lot during measurements close to room temperature. This causes a big voltage drop at the 230 V supply circuit of the SMU. The SMU seems not to be able to compensate this effect fast enough, which leads to charging/decharging effects. However for the analysis of the breakdown voltage V_{bd} the exact shape of the IV curve in this region is not of interest, so this will not influence the results of this particular analysis.
In the breakdown voltages (given by the K-factor, but visually obtained by the sudden increase in current) a clear trend can be observed for the diode, as well as the TelePix2. For decreasing temperature the breakdown voltage is also decreasing. This aligns well with the expected behavior, as with decreasing temperature the mean free path of conduction electrons increases. This increased mean free path allows the electrons to achieve the same amount of kinetic energy in lower electric fields. Additionally the band gap between the valence band and conduction band of silicon is also decreasing with decreasing temperature, which results in valence electrons needing less kinetic energy to cross this gap.
If the IV curves at 20 °C and 30 °C are excluded, also a clear trend for the leakage current is observed. The leakage current is increasing with increasing temperature. This also follows the expectations, as the thermal energy of charge carriers is higher with increasing temperature. This will be analyzed in much more detail in the next section. It should also be mentioned here, that the digital part of the TelePix2 was powered using the adapter shown in Figure 33 with a voltage of 1.8 V. This unfortunately lead to a massive increase in the leakage current. Because of that the absolute leakage currents measured while using this adapter can not be compared with other IV curves.

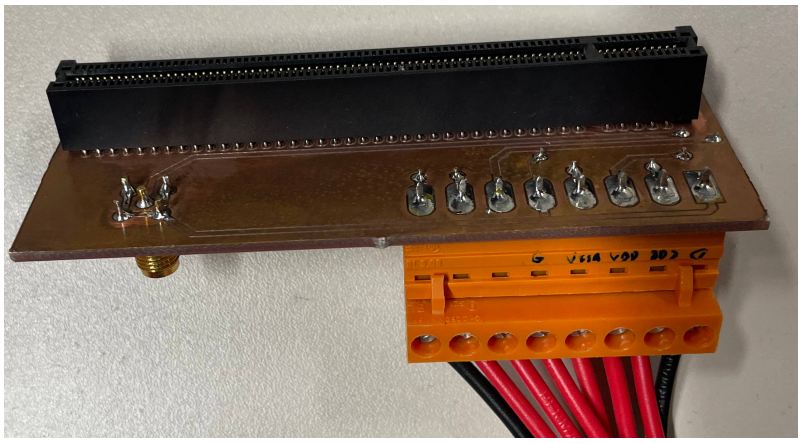

Figure 33: Low voltage power adapter used to power the digital part of the TelePix2 in the climate chamber.

6.2 Temperature dependence of the leakage current

In this second part the temperature dependence of the leakage current will be analyzed in more detail. For this measurements a constant voltage is applied at the chip guard ring. The current is measured again in 1s intervals during the whole duration of the measurement. To track the temperature of the chip, a PT1000 (temperature dependent resistor) is used. It is estimated that the measured temperature is lower than the actual temperature of the chip. Each measurement consists of two parts, first a cooldown sequence and then a warmup sequence. During the cooldown the freezer is set to $-50\,°\mathrm{C}$ and completely closed, while during the warmup the freezer is turned off completely and slightly opened. The measurements are performed for a total of 6 different voltages ranging from $21\,\mathrm{V}$ to $125\,\mathrm{V}$. The electronic readout part of the TelePix2 was powered during the whole measurement, to simulate the actual operation of the chip.
To plot the results, the measurements are binned in $0.1\,°\mathrm{C}$ wide bins. Within these bins the mean and standard deviation are used as error estimation of the current. The resulting statistical error is the only error that was used in the further analysis for the current. For the temperature value a constant error of $\Delta T = 3\,\mathrm{K}$ is taken into account. This error includes the error of the resistance measurement as well as the error of the $T(R)$ function that is used to calculate the temperature from the resistance of the PT1000. The results of such a measurement are shown in Figure 34

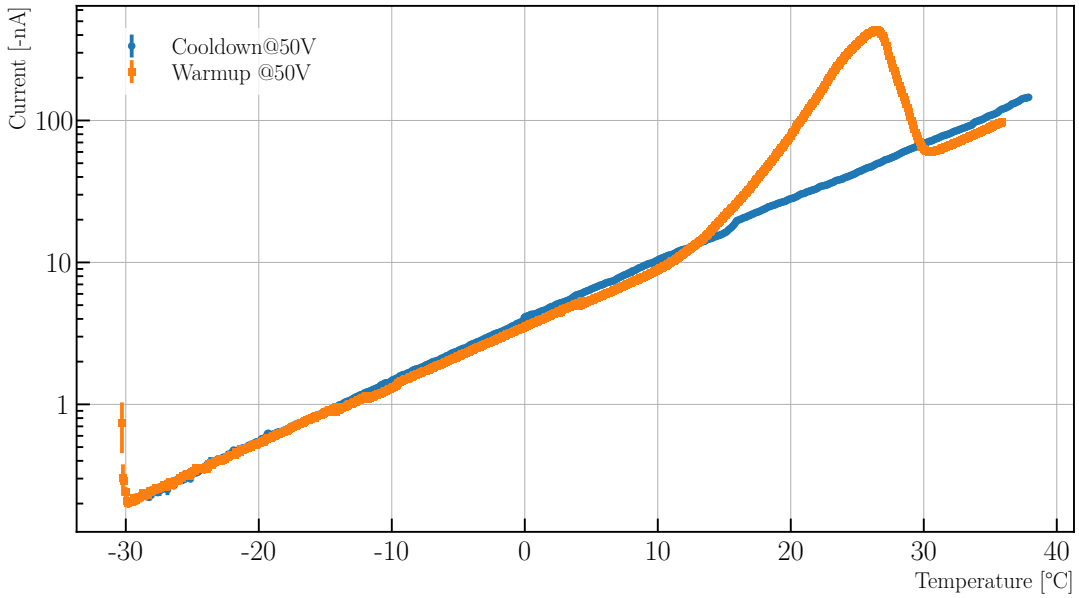

Figure 34: Leakage current of a TelePix2 plotted against the temperature for one cooldown and warmup sequence with 50V bias voltage applied at the chip guard ring

In the plot a peak in the warmup sequence is observed. It is suspected that this peak is the result of condensation on the chip, as during the warmup the freezer is switched off and therefore is not able to work against the increasing humidity, which is a result of hotter air entering the freezer. As this peak was observed in every warmup measurement, only the cooldown measurements are used for further analysis.
It is predicted, that the leakage current is described by (3.22). This is tested on the measured cool down sequences with a bias voltage of 50 V.For this a fit will be performed on the data using (3.22) as a fit function. To simplify the fit a fair bit, the given relation is slightly rearranged:

$$\ln \frac{1}{T^2} \propto -\frac{E_a}{2k_b T}. \tag{6.1}$$

This relation, that turned the exponential fit into a linear fit, is plotted in Figure 35. The linear behavior of the function can clearly be observed. Also the fit seems to describe the data well.

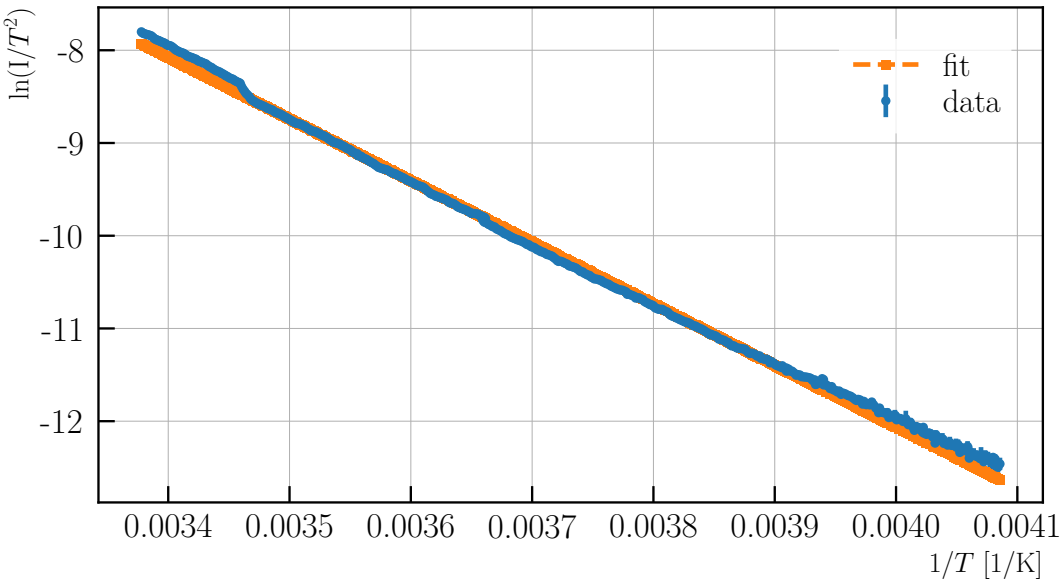

Figure 35: $\ln \frac{1}{T^2}$ plotted as a function of $\frac{E_a}{2k_bT}$ with a fit to describe the data. The data is given by the cooldown sequence shown in Figure 32.

From that fit it is also possible to determine the effective energy E_a. In Table 4 all the values of E_a obtained by fitting the cooldown sequences for different voltages are shown:

Voltage [-V]	E_a [eV]	ΔE_a [eV]
21	1.1827	0.0020
50	1.1452	0.0015
70	1.1453	0.0013
90	1.0760	0.0007
110	1.0146	0.0011
125	0.9748	0.0008

Table 4: Fitted values of the effective energy E_a for different voltages applied at the TelePix2 chip guard ring. The errors of the values are only statistical errors from the fit, systematical errors are not accounted for.

None of the fitted values are directly compatible with the common literature value of $E_{a,lit} = 1.21\,\text{eV}$. However that is mainly caused by the very small errors that the fit produces, which are themselves linked to the very small errors of the measurement itself. These errors are, especially for the current measurement, underestimated, as already discussed earlier.
Additionally a better temperature measurement, ideally directly within the chip, could improve the results by a lot.
Furthermore a trend in the effective energy towards lower values for higher bias voltages is observed. This could be linked to the trap assisted tunneling affecting the leakage current in the transition region, as discussed in subsection 5.3. A correction of the leakage currents voltages in this regions is not done in this section. This could further improve the results.

With the analysis presented in this section it seems valid to approximate HV-MAPS chips as simple diodes with respect to the temperature dependence of their IV curves.

7 Irradiation Effects on the Leakage Current

In this section the effects of ionizing radiation, in particular X-rays, on the leakage current will be investigated. During the operation at LHCb, HV-MAPS will be subjected to ionizing radiation by design. Hence it is important to determine the influence of the irradiation on various components of the chip, to see how the operation is affected. The leakage current during the irradiation is an important characteristic of the active diode part of HV-MAPS and is investigated here.
All irradiation sequences were done in the Phywe X-ray tube described in subsection 4.5. During the irradiation process a constant bias voltage was applied at the chips and the current was measured. In most cases an additional voltage was also tracked (e.g. voltage at the pixel guard ring while biasing over the chip guard ring).

7.1 BeBiPix Irradiation Studies

7.1.1 Currents during and after the Irradiation

First the currents that are measured during the irradiation will be discussed. Before starting the irradiation process of the chips, the carrier board is irradiated, to check whether a significant amount of current is produced by the board absorbing X-ray photons. This was determined to not be the case.
The exact X-ray rate of the tube is not calibrated within the scope of the thesis. Former rate measurements in the tube [38] indicate a rate of about 40 MHz at 0.1 mA X-ray current, which is roughly the rate that is expected at the innermost chips at the LHCb MightyTracker. For more accurate measurements in the future the exact rate of the tube needs to be calibrated. With the geometry that was used to irradiate the chips, it is expected that the majority of the X-rays reaches the depleted zone of the diode.
During the irradiation the BeBiPix is biased using a voltage of $V = -60\,\mathrm{V}$ to achieve a moderate base current level. In all measurements this bias voltage is applied at the chip guard ring.
Typical curves for such an irradiation process with a constant X-ray current are shown in Figure 36. For the plotting purposes again the standard deviation and the mean over 60 measurements (one minute) are utilized.

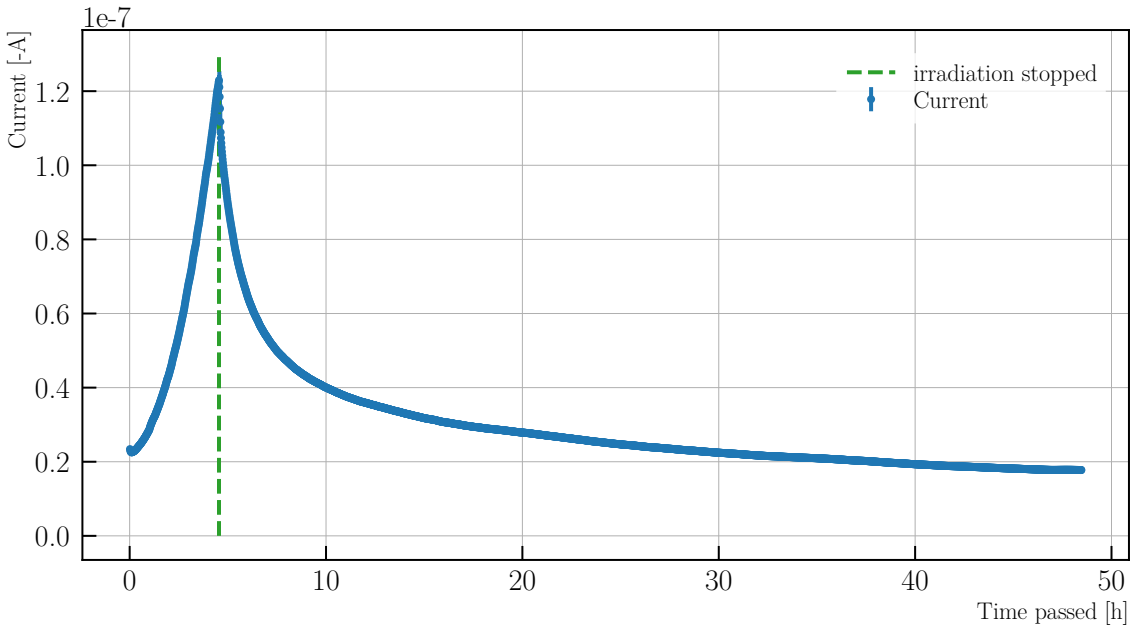

Figure 36: Measured currents of the BeBiPix in the X-ray tube while irradiating with a constant 0.5 mA X-ray current.

In the plot a clear increase in the measured current is observed. After the X-ray tube is turned off again the current drops back down with a rather large time constant. The increase and decrease of the current is now investigated in more detail. The increase can be split into the beam induced current and the leakage current of the chip. The beam induced current is expected be constant during the constant irradiation process, as the rate of X-ray photons hitting the detection volume and converting their energy into a electron-hole pair, is roughly (neglecting the change of the size of the depletion volume) constant. As the size of the BeBiPix is rather small, a small beam induced current is expected.
The beam induced current produced in the BeBiPix is determined by taking a closer look at the points in time where the irradiation started/stopped. In both cases an change of about 10 nA in the measured current is observed (Figure 37,Figure 38).
The source of the increase in leakage current is not fully understood. This is discussed in more detail in subsection 7.3.

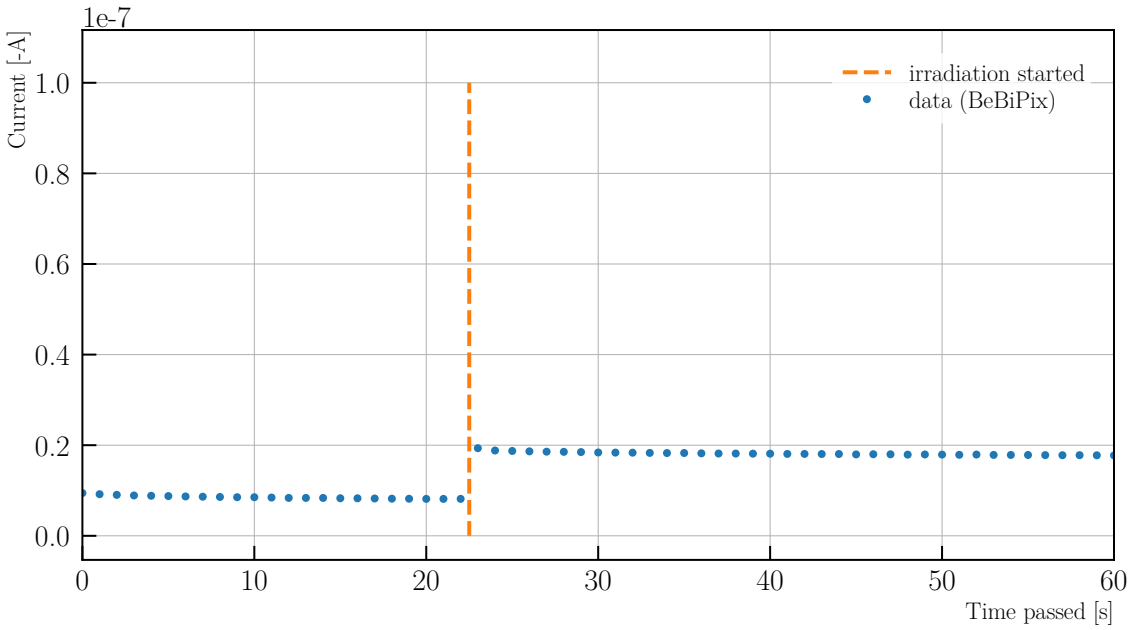

Figure 37: Visualization of the beam induced current in a BeBiPix at the turn on point of the X-ray tube.

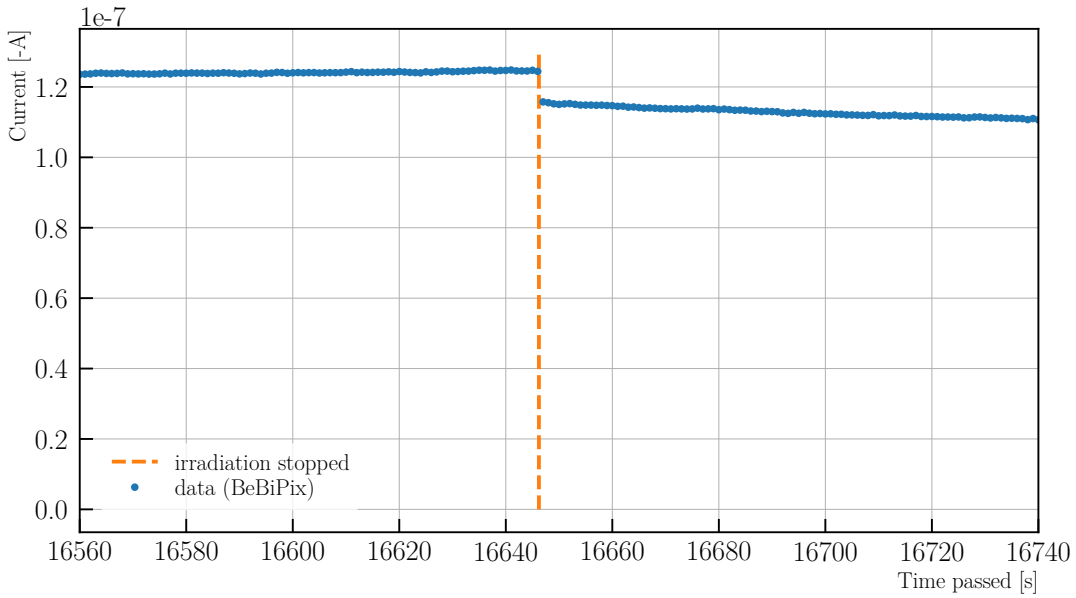

Figure 38: Visualization of the vanish of the beam induced current in a BeBiPix after turning of the X-ray tube.

After the irradiation the chip is still powered and the current is measured. As already mentioned the beam induced current vanishes in an instant after stopping the irradiation. The leakage current also decreases after the irradiation. The exact decay of this current is not understood and can not described by an analytical function within this thesis. The current drop of a BeBiPix after the irradiation is shown in Figure 39

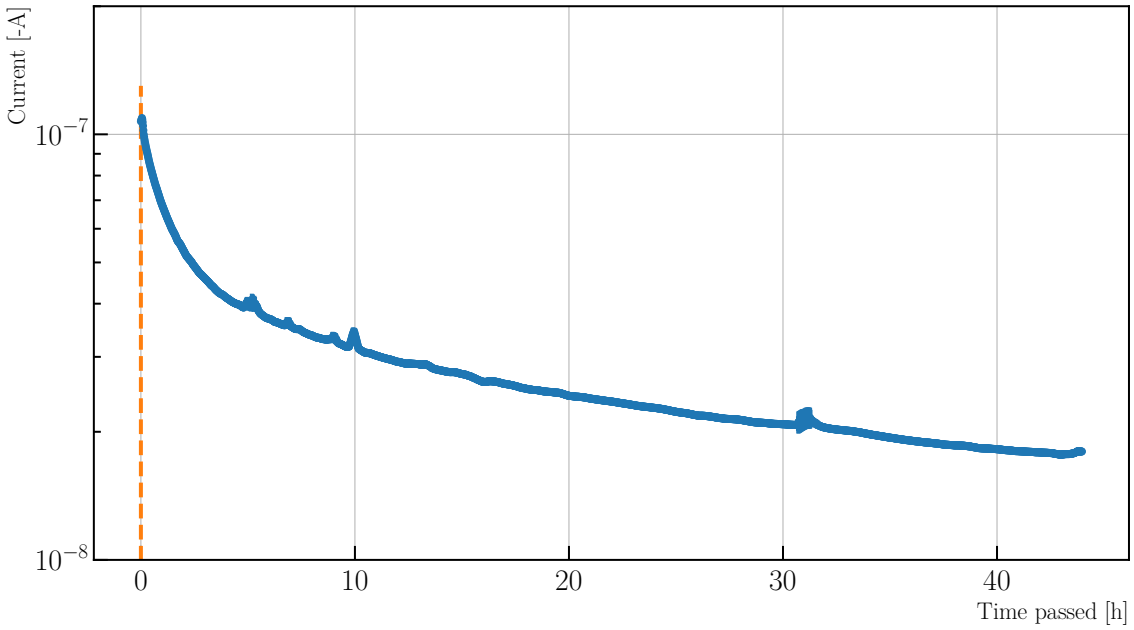

Figure 39: Current of a BeBiPix after the irradiation (logarithmic scale).

7.1.2 Influence of a fixed N guard ring potential

As the BeBiPix features the additional N guard ring contact the influence of a fixed potential at this N ring is studied. For this a carrier board containing two BeBiPix was created (Figure 40).

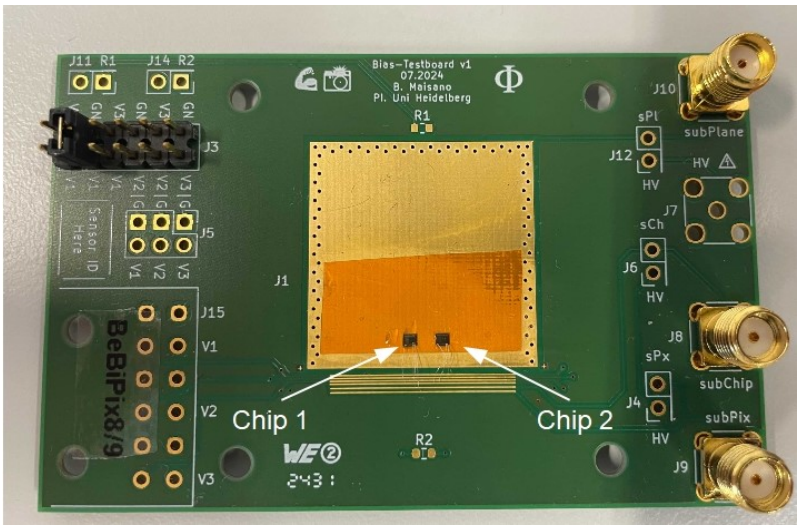

Figure 40: Carrier board with two BeBiPix

Figure 41 shows the currents during the irradiation process of the two BeBiPix.

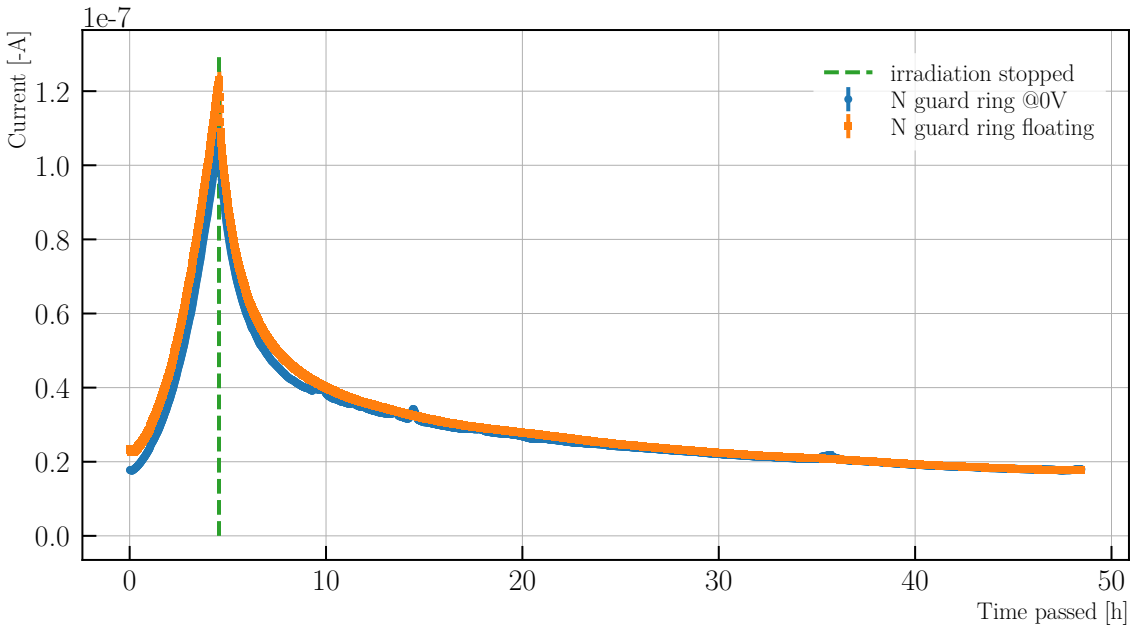

Figure 41: Measured currents of the BeBiPix in the X-ray tube while irradiating with a constant 0.5 mA X-ray current. The data in blue shows the currents in a BeBiPix with a fixed potential of 0 V at the N guard ring. The data shown in orange is taken with a BeBiPix where the N guard ring is not at a fixed potential.

Between the two different data sets, no clear deviation can be observed, which leads to the conclusion, that at least in this specific configuration, no influence of a fixed potential of the N guard ring can be observed.

7.1.3 Currents in consecutive Irradiations

The BeBiPix is irradiated multiple times. Within these measurements significant differences between the first and following irradiation sequences are found. In Figure 42 the difference between the first and second irradiation sequences of a BeBiPix is shown. Both irradiations are carried out at the same X-ray current of 0.5 mA. Between the two measurements the chip is not powered and is resting at room temperature for about 1 day. Only the part of the data, where the X-ray tube is active, is shown.

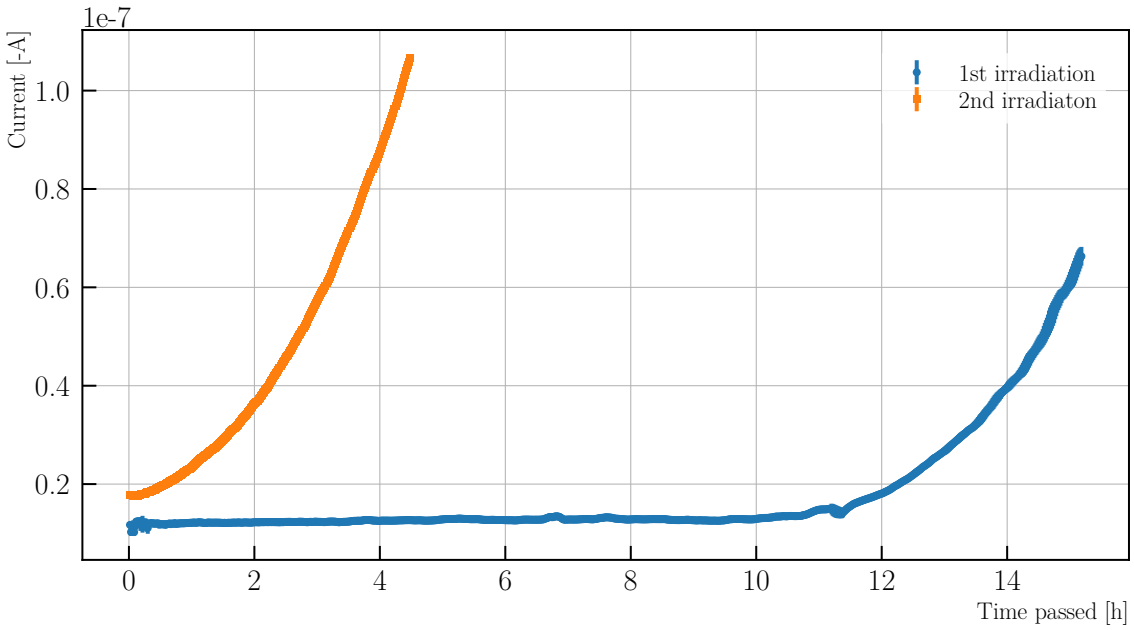

Figure 42: Current over time for the first two irradiations of a BeBiPix with 0.5 mA X-ray current.

Between the two curves there is a big difference concerning the time it takes for the current to increase significantly. During the first irradiation it took roughly 11 h till a significant increase in the current can be observed. During the second irradiation however, the significant increase seems to start right at the beginning of the irradiation. Another difference is the base level of the current. In the second irradiation sequence, this base level is significantly higher than during the first irradiation.

7.1.4 Observations at the Pixel Guard Ring

During the irradiation sequences the potential present at the pixel guard ring V_P is measured, while the bias voltage is supplied through the chip guard ring. In Figure 43 the measured voltage during the first two irradiations is shown. As discussed earlier the chip is biased using the chip guard ring and a bias voltage of -60 V.

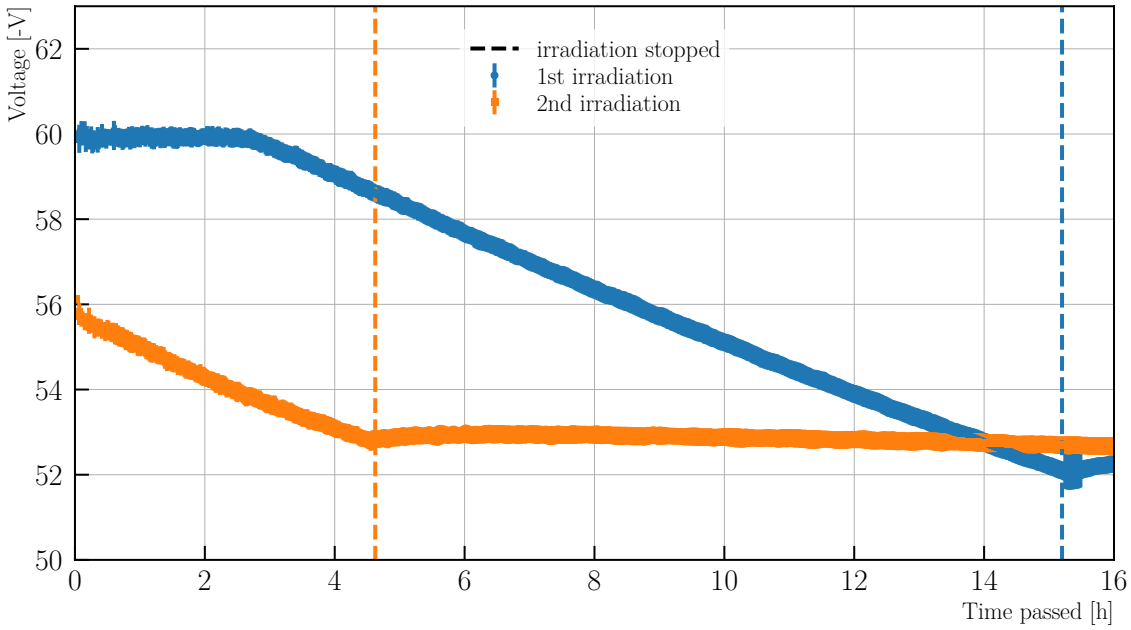

Figure 43: Voltage at the pixel guard ring during the first two irradiations of the BeBiPix with 0.5 mA X-ray current.

In both measurements a linear decrease of the potential at the pixel guard ring is observed. While in the second irradiation this linear decrease starts with no delay after the X-ray tube is turned on, the voltage in the first irradiation stays constant for about 2.5 h.
Furthermore, the base level of the voltage differs significantly in this case. At the start of the first irradiation, the pixel guard ring voltage is at the same level as the at the chip guard ring applied bias voltage.
After stopping the irradiation a slight increase in the voltage is observed in both chips. After this small increase the voltage seems to remain at a constant level.
Between the start of the voltage drop and the start of the increase in the leakage current no timely correlation is observed.

7.2 MightyPix Irradiation Studies

7.2.1 Currents during and after the irradiation

Similar studies are also done with the MightyPix. The MightyPix was biased at the chip guard ring using a bias voltage of $V = -100\,\mathrm{V}$. The resulting currents in a MightyPix during an irradiation with a X-ray current of 0.5 mA are shown in Figure 44. The beam induced current is analyzed similarly to the procedure for the BeBiPix. In this case a beam induced current of 150 nA is found. As this measurement unfortunately ended early, due to technical difficulties, another measurement, this time with a X-ray current of 1 mA, is carried out. With this higher current it is suspected to amplify observed effects, as previously observed with the BeBiPix.

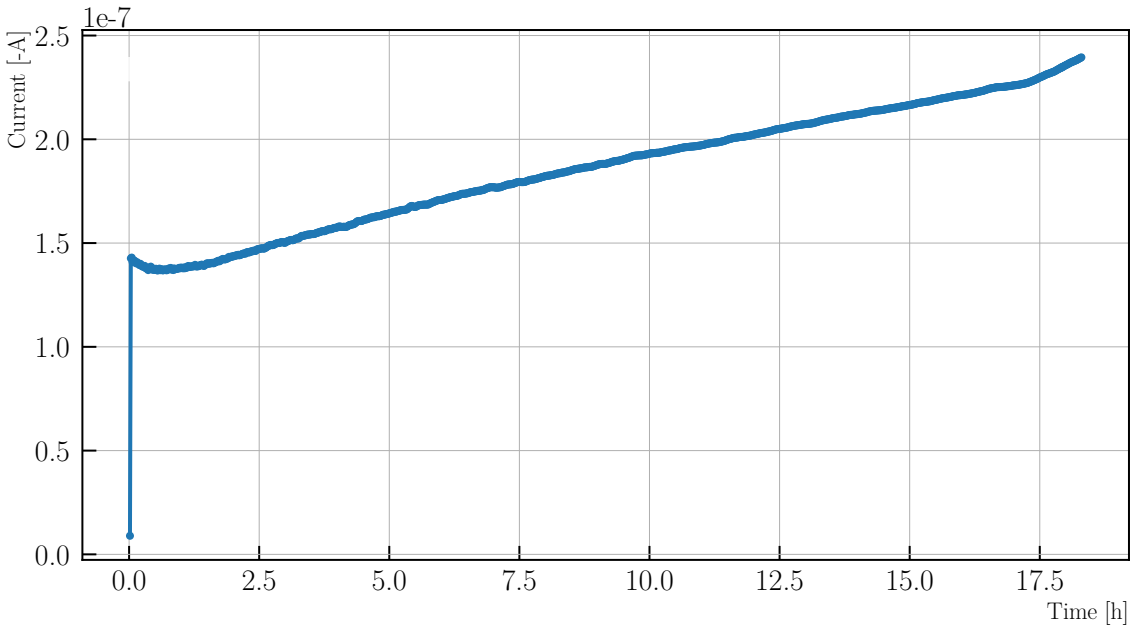

Figure 44: Current during the first irradiation of a MightyPix with 0.5 mA X-ray current.

The currents observed during this second irradiation are shown in Figure 45

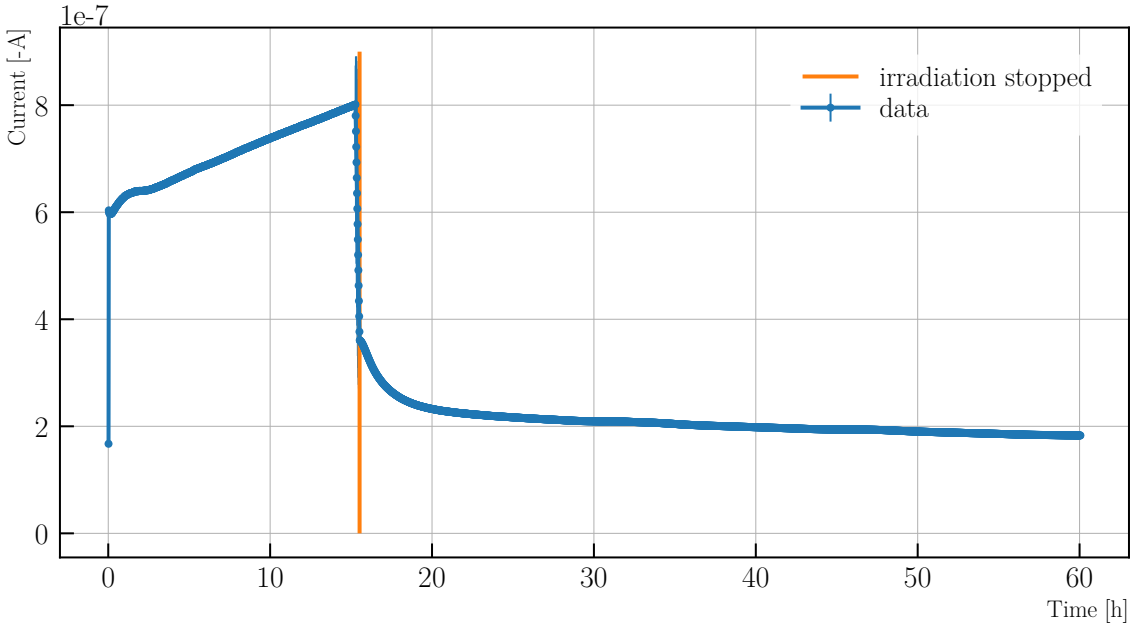

Figure 45: Current during and after the second irradiation of a MightyPix with 1 mA X-ray current.

In this case a beam induced current of around 440 nA is observed in the plot (jump at the beginning and after stopping the irradiation). This is roughly in the order of what is expected from the beam induced current observed in the BeBiPix, taking the different chip sizes and Xray currents into account.
During the irradiation a linear increase additionally to the beam induced current is

observed. At the start of the irradiation a small deviation from the linear increase can be observed.
After the irradiation stops, the beam induced current again vanishes in an instant. Again the leakage current decays after the irradiation.
Another thing that should be mentioned here, is that the base level of the current was significantly higher before the second irradiation compared to the first irradiation.

7.2.2 Observations at the Pixel Guard Ring

During the second irradiation of the MightyPix the voltage at the pixel guard ring is tracked as well (see Figure 46). Similar effects as in the BeBiPix are observed in this case. Again a linear decrease of the voltage during the irradiation can be observed. After the irradiation a small increase in the voltage is observed, after which the pixel guard ring voltage stays constant.

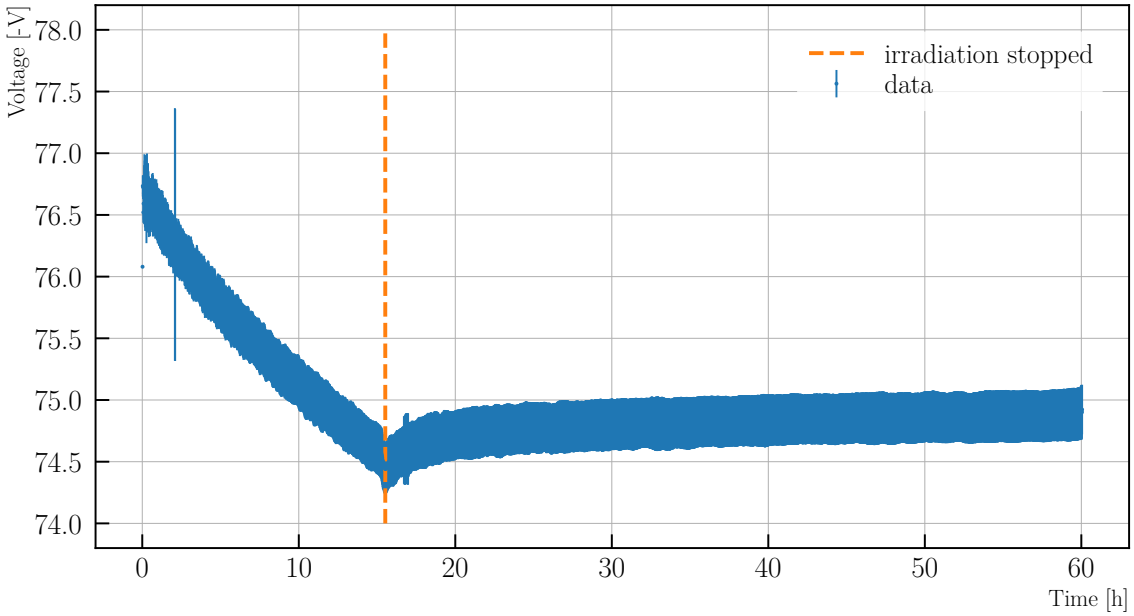

Figure 46: Pixel guard ring voltage during and after the second irradiation of a MightyPix with 1 mA X-ray current.

7.3 Conclusion on Irradiation Effects

A lot of different effects are observed during the irradiation of different chips with X-rays. Similar effects can be observed in both the pixel guard ring voltage and the leakage current across different chips.
In all cases a beam induced current can be observed. The amount of beam induced current follows the expectations to a certain degree. In the MightyPix (chip size: $5 \times 20\,\mathrm{mm}^2$) the leakage current is substantially higher than in the smaller (chip size: $1.2 \times 1.3\,\mathrm{mm}^2$) BeBiPix. Also for a higher X-ray current the beam induced current is higher, as observed in the MightyPix. It is expected, that at double the X-ray current (rate) the beam induced current would also double. This does not hold true (150 nA vs 440 nA)for the beam induced current measured with the MightyPix. A

possible reason for that is a different position in the X-ray tube. A deeper analysis with exact and position dependent rate measurements is needed to determine this in more detail.
The increase in leakage current during the irradiation is not fully understood within this thesis, though some possible sources for this are now discussed. The IEL damage the X-rays produce is expected to manifest as trapped holes in the SiO_2-Si transition region. These regions are especially found within the pixels, where the electronic readout of the chips is located. The trapped holes alter the exact structure of the electric fields in the pixels. How this alteration looks exactly can not be determined within the scope of this thesis. For that extensive simulations of this trapped hole accumulation are needed. It is suspected however, that the alteration of the field structure leads to similar effects that are utilized in a FET transistor. The accumulated charges would serve as the gate voltage in a transistor. As the accumulated charge of the trapped holes increases with time during the irradiation, so does the gate voltage, which leads to an increase in the flowing current. A strong indication for this effect is the delayed current increase in the first irradiation. It seems like first a certain threshold potential (number of trapped holes) needs to be reached before the leakage current can increase significantly. An analysis of whether it is possible to return to the original state of the chip via annealing, could verify this.
The drop in the current after the irradiation is probably linked to the decay of trapped holes. This decay happens if free electrons recombine with the trapped holes. The exact decay process of this holes is not understood. However several effects indicate that not all of these holes can decay after the irradiation. In the second irradiation sequence no delay of the current increase can be observed. Also the base current level is higher in the second irradiation. This can be explained by non decaying trapped holes from the former irradiation. As this is not observed in the MightyPix it is suspected that the different production processes also influence these effects. To analyze this in more details again simulations and more measurements with different configurations are needed.
The last effect that is discussed here is the voltage drop at the pixel guard ring. The voltage present at the pixel guard ring is linked close to the exact electric field structure in the pixel. Therefore it is not unexpected that the voltage at the pixel guard ring changes during the irradiation. What is not predicted however is that the pixel guard ring voltage drop does not recover after the irradiation. Intuitively a change in this voltage would be expected from the decay of the holes and change in the potential. The exact dependence of the pixel guard ring voltage on the trapped charges can probably be extracted from a simulation of the irradiation process.
It should be noted that the increase in leakage current produced by IEL is significantly lower than the observed increase in leakage current as a result of NIEL damage [39, 40].

8 Conclusion and Outlook

In this thesis several aspects of the leakage current in the active diode part of different HV-MAPS chips are examined. As the leakage current greatly influences the noise level of HV-MAPS, the IV characteristic and influences of temperature and radiation damage are an important characterization tool.

First the general behavior of the IV characteristic is analyzed. Within this characteristic curve three different regions can be defined. The depletion region, where the leakage current obeys the relation $I \propto \sqrt{V}$, a transition region, where additional leakage current is produced and finally the breakdown. It is suspected that the additional leakage current in the transition region is a result of trap assisted tunneling. The observed breakdown likely follows the behavior of an avalanche breakdown. Moreover, there is evidence that the breakdown happens in the pixel matrix between the deep N well and pixel guard ring. For each region a model description is given and tested against the data. A good compatibility between the assumed theoretical description and measured data is observed. It is concluded that the main component of the leakage current present in HV-MAPS originates in the depleted zone within the pixel matrix.

In the next part of this thesis the temperature dependence of the leakage current is investigated. First a temperature dependence of the breakdown voltage V_{bd} is observed. This temperature dependence is explained by the fact that the mean free path of conduction electrons increases with decreasing temperature. At low temperatures these conduction electrons can gather more kinetic energy between interactions, which leads to an avalanche breakdown at a lower bias voltage.

The analysis of the temperature dependence of the leakage current again yields a good compatibility with the expected behavior. The effective energy E_a is determined from the temperature dependence of the leakage current. For bias voltages in the depletion region a small deviation from the literature value $E_a = 1.21\,\mathrm{eV}$ is observed, which is explained by the underestimation of systematical errors within the analysis. For higher bias voltages inside the transition region a decrease in the effective energy is observed. It is believed that this behavior is a result of trap assisted tunneling as well as leakage current in the so-called transition region.

In the last part of this thesis the effects of IEL damage, in this case X-rays, on the leakage current and electric field structure within the chip are investigated. During the irradiation an increase in the current is observed. This increase can be split into a beam induced current and an actual increase in the leakage current. To gain insights in the electric field structure in the chip, the pixel guard ring voltage is tracked during the irradiation, while the bias voltage is applied at the chip guard ring. For the voltage at the pixel guard ring a linear decrease is found during the irradiation. The increase in leakage current and the drop in voltage is suspected to be a result of trapped holes in the SiO_2-Si transition region, which affect the structure of the electric fields within the pixels. The exact effect can not be determined in detail within this thesis. For this a simulation of the trapped hole accumulation is needed. It is found that the increase in leakage current produced by this IEL damage is lower than the leakage current produced by NIEL damage during operation in the LHCb MightyTracker.

To further improve the understanding of the leakage current in HV-MAPS, several steps can be implemented by future analysis. One important tool to understand the

effects of IEL damage on the leakage current, could be TCAD simulations of the damage. With that it should be possible to predict exactly how the electric field structure in the pixels is affected by the accumulation of trapped holes. Furthermore it should be possible to simulate the influence of the leakage current. For further refining this understanding, more IEL damage inducing irradiation of chip samples can be done. In detail measurements at a higher total dose and rate will be needed to gain deeper insights in the IEL damage. Additionally irradiations using electrons or protons as a source of IEL damage could give insights into IEL damage that will be produced in the MightyTracker.
It will also be interesting to analyze the leakage currents of new HV-MAPS prototypes to compare whether similar characteristics are present. IV characteristic can also be used as a quality control instance for commissioning chips for the use in the experiment.

Bibliography

[1] P. W. Higgs. „Broken Symmetries and the Masses of Gauge Bosons“. In: *Phys. Rev. Lett.* 13 (16 Oct. 1964), pp. 508–509. DOI: 10.1103/PhysRevLett.13.508. URL: https://link.aps.org/doi/10.1103/PhysRevLett.13.508.

[2] ATLAS Collaboration. „Observation of a new particle in the search for the Standard Model Higgs boson with the ATLAS detector at the LHC“. In: *Physics Letters B* 716.1 (Sept. 2012), pp. 1–29. ISSN: 0370-2693. DOI: 10.1016/j.physletb.2012.08.020.

[3] CMS Collaboration. „Observation of a new boson at a mass of 125 GeV with the CMS experiment at the LHC“. In: *Physics Letters B* 716.1 (Sept. 2012), pp. 30–61. ISSN: 0370-2693. DOI: 10.1016/j.physletb.2012.08.021.

[4] A. D. Sakharov. „Violation ofCPin variance,Casymmetry, and baryon asymmetry of the universe“. In: *Soviet Physics Uspekhi* 34.5 (May 1991), pp. 392–393. ISSN: 0038-5670. DOI: 10.1070/pu1991v034n05abeh002497.

[5] Y. Fukuda et al. „Measurements of the Solar Neutrino Flux from Super-Kamiokande's First 300 Days“. In: *Physical Review Letters* 81.6 (Aug. 1998), pp. 1158–1162. ISSN: 1079-7114. DOI: 10.1103/physrevlett.81.1158.

[6] O. Brüning and L. Rossi. „High-Luminosity Large Hadron Collider“. en. In: *CERN Yellow Reports: Monographs* (2020), Vol. 10 (2020): High–Luminosity Large Hadron Collider (HL. DOI: 10.23731/CYRM-2020-0010.1.

[7] LHCb Xollaboration. *Physics case for an LHCb Upgrade II - Opportunities in flavour physics, and beyond, in the HL-LHC era*. 2019. arXiv: 1808.08865 [hep-ex]. URL: https://arxiv.org/abs/1808.08865.

[8] I. Perić. „A novel monolithic pixelated particle detector implemented in high-voltage CMOS technology“. In: *Nuclear Instruments and Methods in Physics Research Section A: Accelerators, Spectrometers, Detectors and Associated Equipment* 582.3 (2007). VERTEX 2006, pp. 876–885. ISSN: 0168-9002. DOI: https://doi.org/10.1016/j.nima.2007.07.115. URL: https://www.sciencedirect.com/science/article/pii/S0168900207015914.

[9] LHCb Collaboration. „LHCb Tracker Upgrade Technical Design Report“. In: (Feb. 2014).

[10] M. E. Peskin. *An introduction to quantum field theory*. Ed. by D. V. Schroeder. The advanced book program. Description based upon print version of record. Boulder, Co.: Westview Press, 1995. 1842 pp. ISBN: 9780813345437.

[11] Wikipedia Commons. *Standard Model of Elementary Particles*. URL: https://en.wikipedia.org/wiki/File:Standard_Model_of_Elementary_Particles.svg.

[12] N. Cabibbo. „Unitary Symmetry and Leptonic Decays“. In: *Physical Review Letters* 10.12 (June 1963), pp. 531–533. ISSN: 0031-9007. DOI: 10.1103/physrevlett.10.531.

[13] M. Kobayashi and T. Maskawa. „CP-Violation in the Renormalizable Theory of Weak Interaction“. In: *Progress of Theoretical Physics* 49.2 (Feb. 1973), pp. 652–657. ISSN: 0033-068X. DOI: 10.1143/ptp.49.652.

[14] LHCb Collaboration. „Framework TDR for the LHCb Upgrade II. Opportunities in flavour physics, and beyond, in the HL-LHC era“. In: (Feb. 2022).

[15] S. Bachmann and L. Dittmann. *Pixel sensor specifications for theLHCb MightyPixel tracker*. Physikalisches Institut Heidelberg, Oct. 2024.

[16] S. Navas et al. „Review of particle physics“. In: *Phys. Rev. D* 110.3 (2024), p. 030001. DOI: 10.1103/PhysRevD.110.030001.

[17] H. Kolanoski. *Particle Detectors. Fundamentals and Applications*. Ed. by N. Wermes. Description based on publisher supplied metadata and other sources. Oxford: Oxford University Press USA - OSO, 2020. 1949 pp. ISBN: 9780191899232.

[18] S. Hunklinger and C. Enss. *Festkörperphysik*. De Gruyter, Oct. 2023. ISBN: 9783111027227. DOI: 10.1515/9783111027227.

[19] WikipediaCommons. *Pn-junction-equilibrium*. URL: https://en.wikipedia.org/wiki/File:Pn-junction-equilibrium.png.

[20] G. Lutz. *Semiconductor Radiation Detectors*. Springer Berlin Heidelberg, 2007. ISBN: 9783540716792. DOI: 10.1007/978-3-540-71679-2.

[21] M. A. Green. „Intrinsic concentration, effective densities of states, and effective mass in silicon“. In: *Journal of Applied Physics* 67.6 (Mar. 1990), pp. 2944–2954. ISSN: 1089-7550. DOI: 10.1063/1.345414.

[22] N. Bacchetta et al. „Improvement in breakdown characteristics with multiguard structures in microstrip silicon detectors for CMS“. In: *Nuclear Instruments and Methods in Physics Research Section A: Accelerators, Spectrometers, Detectors and Associated Equipment* 461.1–3 (Apr. 2001), pp. 204–206. ISSN: 0168-9002. DOI: 10.1016/s0168-9002(00)01207-9.

[23] D. Groom. „Temperature dependence of mean number of of e-h pairs per eV of x-ray energy deposit“. In: (Dec. 14, 2004).

[24] L. Dittmann. private communication. 2024.

[25] J. Zhang. „X-ray Radiation Damage Studiesand Design of a Silicon Pixel Sensorfor Science at the XFEL“. PhD thesis. Universität Hamburg, 2013.

[26] L. Rossi. *Pixel Detectors. From Fundamentals to Applications*. Ed. by P. Fischer et al. 1st ed. Particle Acceleration and Detection Ser. Description based on publisher supplied metadata and other sources. Berlin, Heidelberg: Springer Berlin / Heidelberg, 2006. 1315 pp. ISBN: 9783540283331.

[27] Tektronix. *Series 2600B System SourceMeter® Instrument, Reference Manual*. Tektronix. Aug. 2016. URL: https://download.tek.com/manual/2600BS-901-01_C_Aug_2016_2.pdf.

[28] Tektronix. *Model 2000 Multimeter User's Manual*. Tektronix. Aug. 2010. URL: https://download.tek.com/manual/2000-900_J-Aug2010_User.pdf.

[29] Rohde&Schwarz. *R&S®NGE100B Power Supply User Manual*. Rohde & Schwarz GmbH & Co. KG. 2023. URL: https://scdn.rohde-schwarz.com/ur/pws/dl_downloads/pdm/cl_manuals/user_manual/5601_1343_01/NGE100B_User_Manual_en_10.pdf.

[30] Rohde&Schwarz. *R& S®HMP Series Power Supplies Getting Started*. Rohde & Schwarz GmbH & Co. KG. 2022. URL: https://scdn.rohde-schwarz.com/ur/pws/dl_downloads/pdm/cl_manuals/getting_started/1178_6791_01/HMPSeries_GettingStarted_en_03.pdf.

[31] Elcold Frysere Hobro ApS. *ELCOLD UNI Freezers*. ELCOLD. Løgstørvej 81, HørbyDK-9500 HobroDenmark. URL: https://www.elcold.com/GB/PRODUCTS/LOW%20TEMPERATURE%20FREEZERS/UNI.aspx.

[32] Binder GmbH. *Environmental simulation*. URL: https://www.binder-world.com/int-en/products/environmental-testing/.

[33] Phywe Systeme GmbH & Co.KG. *XR 4.0 expert unit, Röntgengerät, 35kV*. Tech. rep. Göttingen: Phywe Systeme GmbH & Co.KG. URL: https://www.phywe.de/physik/moderne-physik/roentgenphysik/xr-4-0-expert-unit-roentgengeraet-35-kv_1557_2488/.

[34] L. Loaiza et al. „Feasibility study of a TIMEPIX detector for mammography applications". In: *13th International Conference on Medical Information Processing and Analysis*. Ed. by J. Brieva et al. SPIE, Nov. 2017, p. 30. DOI: 10.1117/12.2285910.

[35] R. Kolb. „Disentangling the Diffusive Part of the Drift-Dominated Signal Generation in a High-Ohmic Run2021v2 HV-MAPS Prototype". MA thesis. Universität Heidelberg.

[36] E. Garutti and Y. Musienko. „Radiation damage of SiPMs". In: *Nuclear Instruments and Methods in Physics Research Section A: Accelerators, Spectrometers, Detectors and Associated Equipment* 926 (May 2019), pp. 69–84. ISSN: 0168-9002. DOI: 10.1016/j.nima.2018.10.191.

[37] G. Hurkx et al. „A new analytical diode model including tunneling and avalanche breakdown". In: *IEEE Transactions on Electron Devices* 39.9 (1992), pp. 2090–2098. ISSN: 0018-9383. DOI: 10.1109/16.155882.

[38] L. Dittmann. „Tests of an HV-CMOS Prototype for the LHCb MightyTracker". MA thesis. Universität Heidelberg, 2022.

[39] M. Moll. „Radiation Damage in Silicon Particle Detectors". PhD thesis. Universität Hamburg, 1999.

[40] A. Hekert. „Characterization of a Monolithic Pixel Sensor Prototype in HV-CMOS Technology for the High-Luminosity LHC". PhD thesis. Universität Heidelberg, 2020.

A K-Factor Analysis

Additional plots for the K-factor Analysis of different chips are shown here.

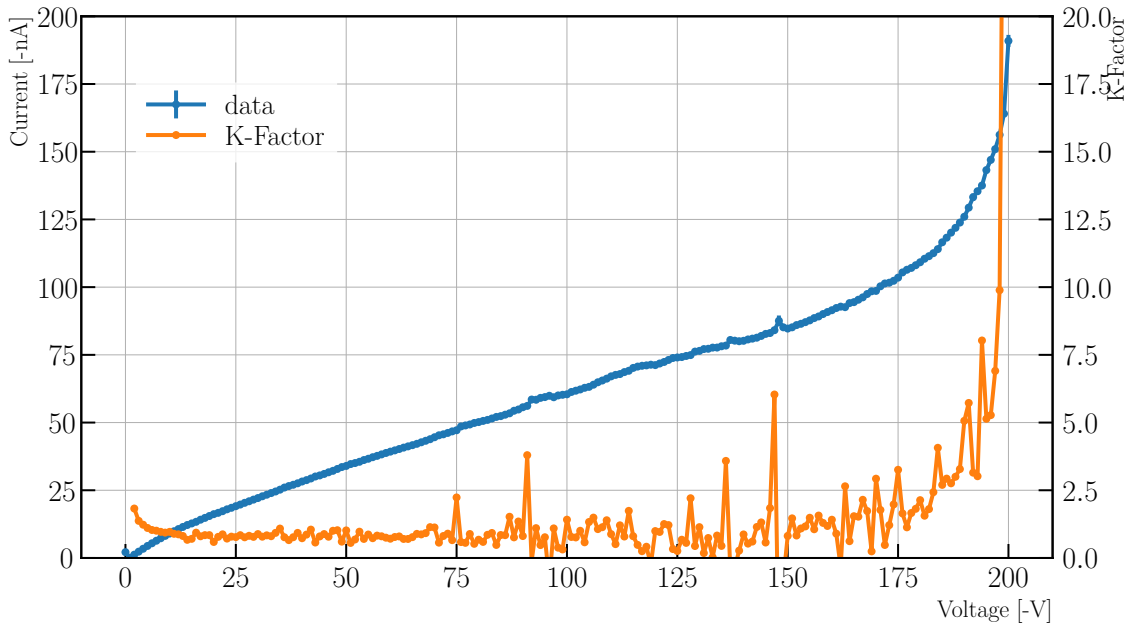

Figure 47: K-factor analysis of a chip guard ring biased MightyPix.

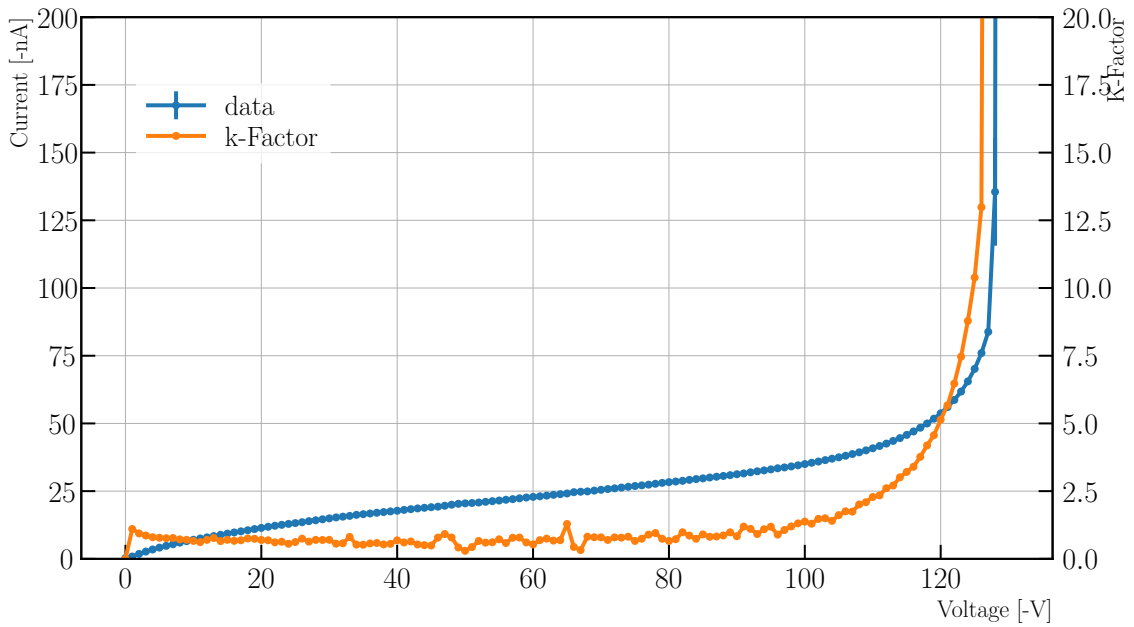

Figure 48: K-factor analysis of a pixel guard ring biased MightyPix.

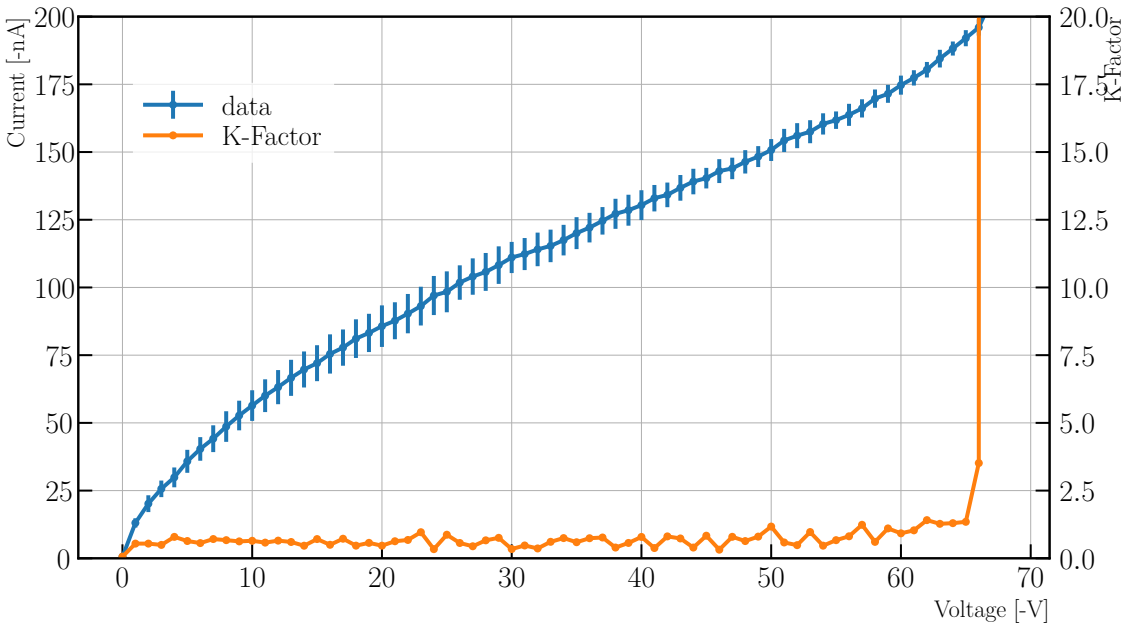

Figure 49: K-factor analysis of a chip guard ring biased AtlasPix3.1.

B IV Fits

Additional plots for IV fits using $I(V) = I_0 + a\sqrt{V} + b\Theta(V - V_T)V^{3/2}\exp(cV)^2$. This is shown again for IV curves of the MightyPix with chip guard ring, pixel guard ring and backside biasing. As well as the AtlasPix3.1 with chip guard ring biasing.

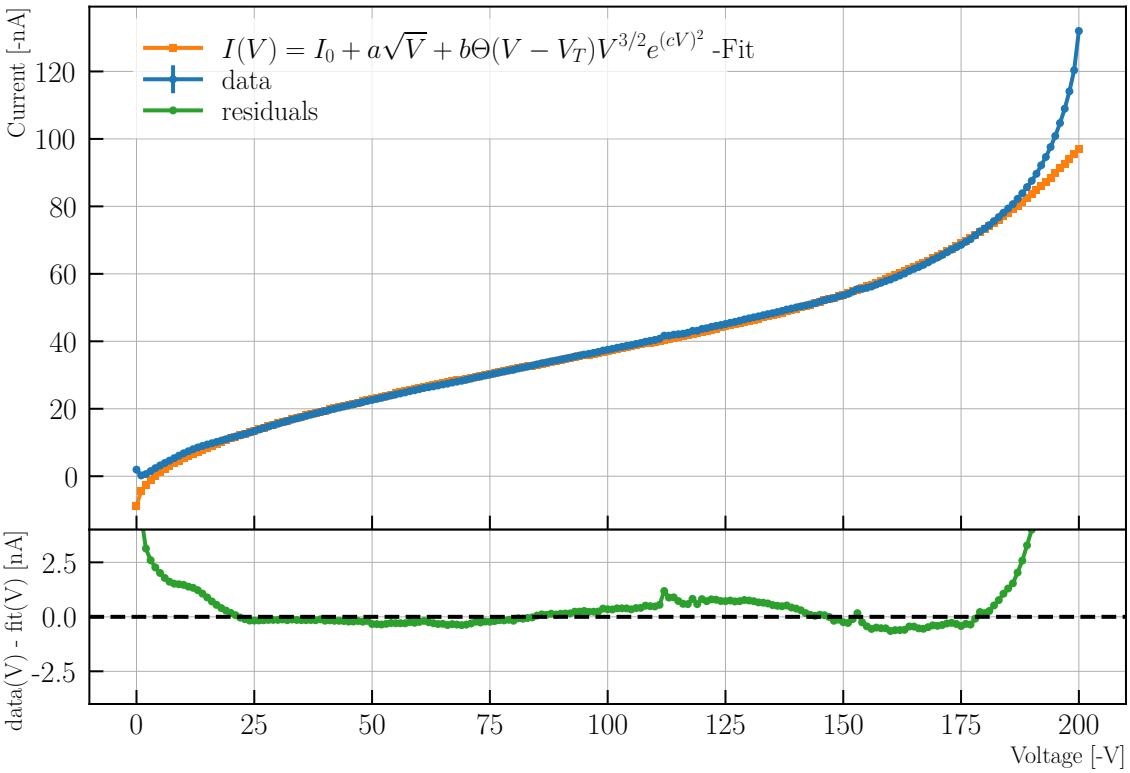

Figure 50: IV-Fit on the IV curve of a MightyPix with backside biasing.

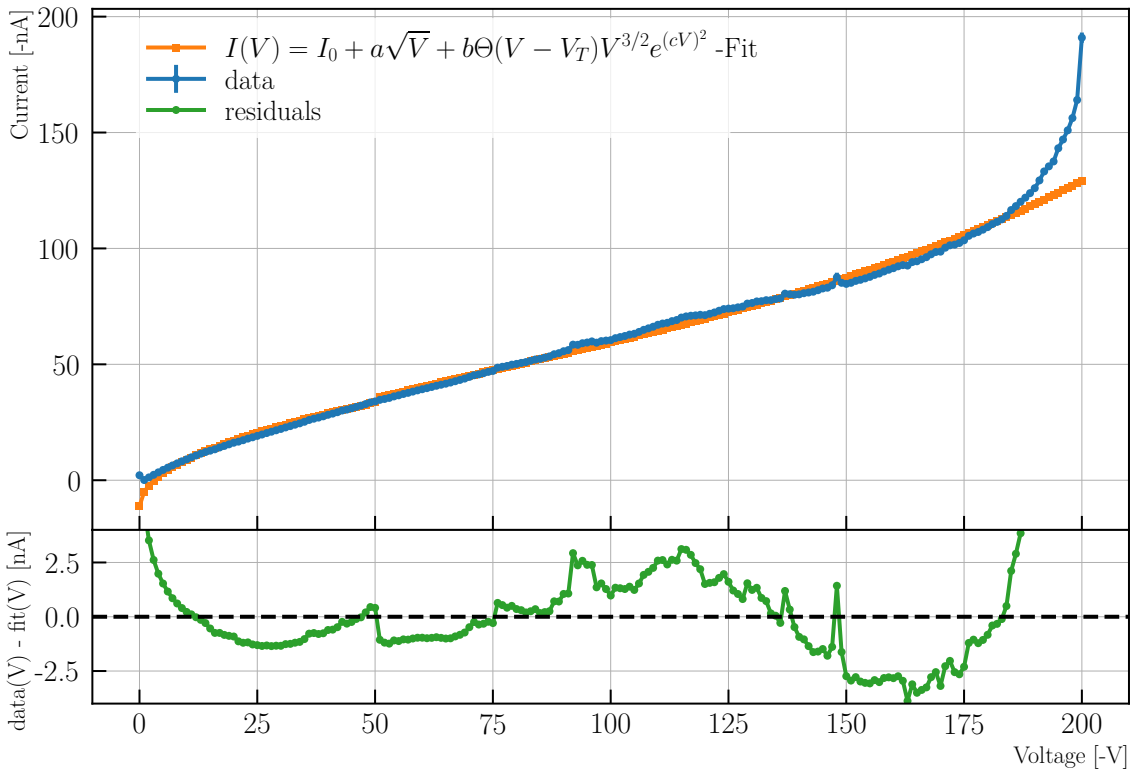

Figure 51: IV-Fit on the IV curve of a MightyPix with chip guard ring biasing.

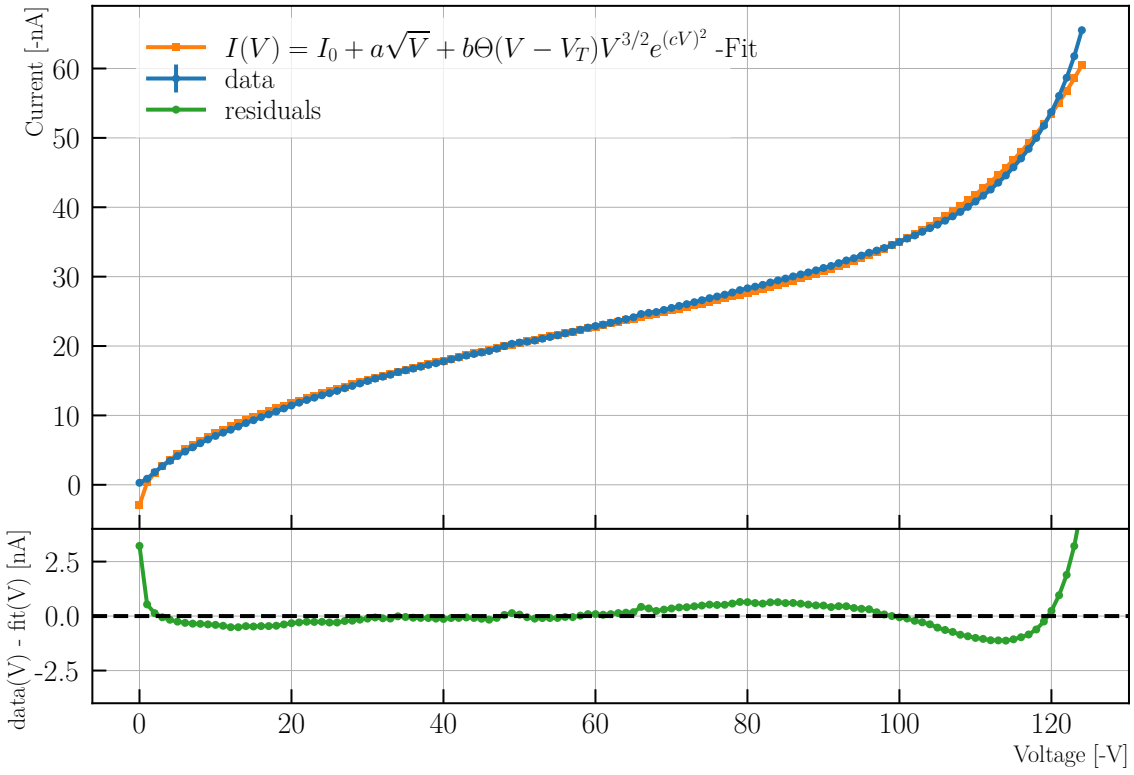

Figure 52: IV-Fit on the IV curve of a MightyPix with pixel guard ring biasing.

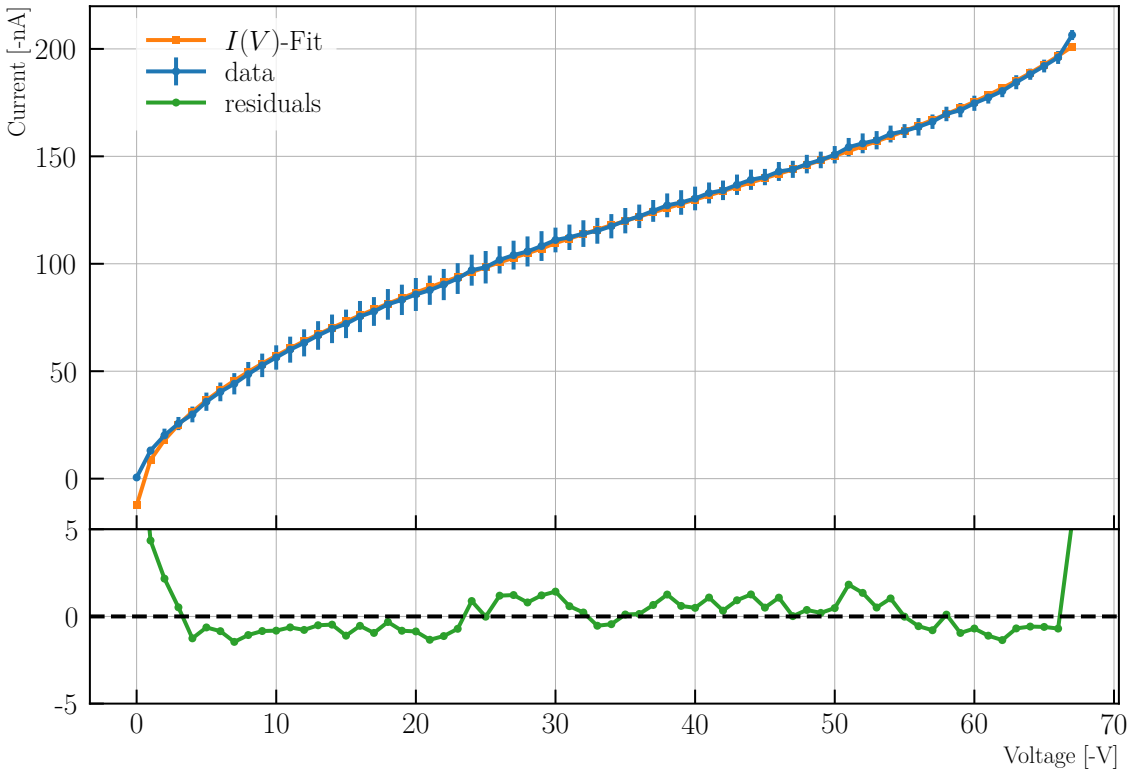

Figure 53: IV-Fit on the IV curve of a AtlasPix3.1 with chip guard ring biasing.

Acknowledgments

First of all I would like to thank Prof. Ulrich Uwer for giving me the opportunity to work on this interesting research topic within the LHCb Heidelberg group. Thanks to Dr.Priv.-Doz. Kai Schweda for kindly agreeing to be the second examiner of my thesis.

Big thanks to Lucas and Sebastian, for their outstanding supervision, their patience in answering my countless questions and their guidance through the whole project.

I would also like to extend my gratitude to Heiko, Ruben, David, Benni, and the rest of the Heidelberg HV-MAPS team for the many insightful discussions on HV-MAPS topics.
Also I would like to thank Benni for giving me the opportunity to work with the BeBiPix.

I am deeply grateful to everyone who took the time to proofread my thesis: Lucas, Ruben, Bene, and Sebastian.

Erklärung

Ich versichere, dass ich diese Arbeit selbstständig verfasst und keine anderen als die angegebenen Quellen und Hilfsmittel benutzt habe.

Heidelberg, den 12.12.2024,

David Kuhn